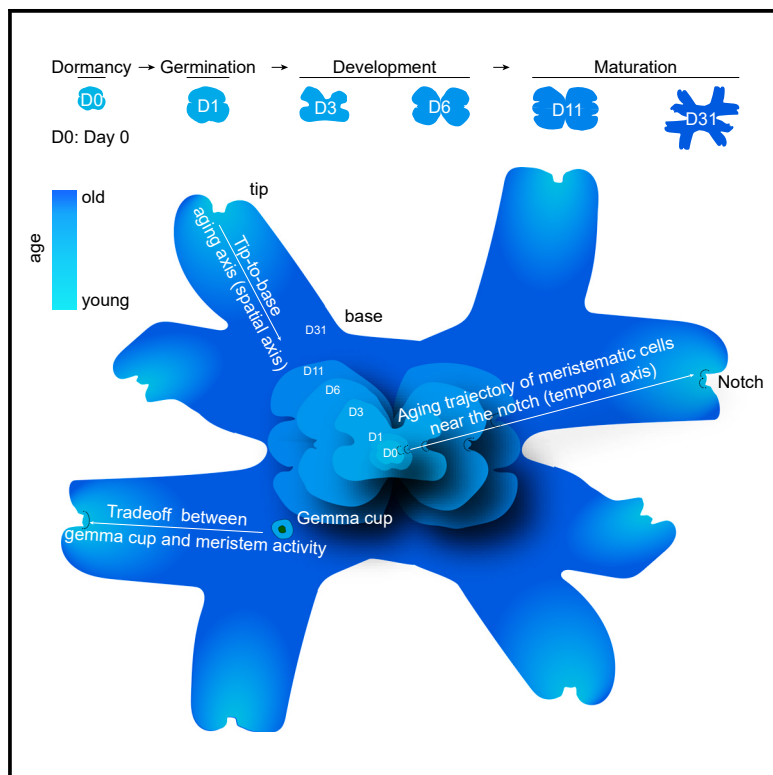


Developmental Cell

The maturation and aging trajectory of *Marchantia polymorpha* at single-cell resolution

Graphical abstract



Authors

Long Wang, Mu-Chun Wan,
Ren-Yu Liao, ..., Hao-Chen Xue,
Yan-Xia Mai, Jia-Wei Wang

Correspondence

jwwang@sippe.ac.cn

In brief

Wang et al. profile transcriptomes of dormant gemmae and developing thalli of different stages at single-cell resolution, defining two maturation and aging axes of the main plant body of *M. polymorpha*. The inference of continuous developmental trajectories for each cell type provides insight into the maturation program of *M. polymorpha*.

Highlights

- We generate a reference cell census for bryophytes
- The collection of cell-type-specific genes accelerates gene discovery
- We define the maturation and aging trajectory of *M. polymorpha* at single-cell resolution
- The vigor of parent plants is determined by the number of offspring



Resource

The maturation and aging trajectory of *Marchantia polymorpha* at single-cell resolution

Long Wang,¹ Mu-Chun Wan,^{1,2} Ren-Yu Liao,^{1,3} Jie Xu,¹ Zhou-Geng Xu,^{1,3} Hao-Chen Xue,^{1,3} Yan-Xia Mai,^{1,4} and Jia-Wei Wang^{1,2,5,*}

¹National Key Laboratory of Plant Molecular Genetics (NKLPMG), CAS Center for Excellence in Molecular Plant Sciences (CEMPS), Institute of Plant Physiology and Ecology (SIPPE), Chinese Academy of Sciences (CAS), Shanghai 200032, China

²School of Life Science and Technology, ShanghaiTech University, Shanghai 201210, China

³University of Chinese Academy of Sciences, Shanghai 200032, China

⁴Core Facility Center of CEMPS, SIPPE, CAS, Shanghai 200032, China

⁵Lead contact

*Correspondence: jwang@sippe.ac.cn

<https://doi.org/10.1016/j.devcel.2023.05.014>

SUMMARY

Bryophytes represent a sister to the rest of land plants. Despite their evolutionary importance and relatively simple body plan, a comprehensive understanding of the cell types and transcriptional states that underpin the temporal development of bryophytes has not been achieved. Using time-resolved single-cell RNA sequencing, we define the cellular taxonomy of *Marchantia polymorpha* across asexual reproduction phases. We identify two maturation and aging trajectories of the main plant body of *M. polymorpha* at single-cell resolution: the gradual maturation of tissues and organs along the tip-to-base axis of the midvein and the progressive decline of meristem activities in the tip along the chronological axis. Specifically, we observe that the latter aging axis is temporally correlated with the formation of clonal propagules, suggesting an ancient strategy to optimize allocation of resources to producing offspring. Our work thus provides insights into the cellular heterogeneity that underpins the temporal development and aging of bryophytes.

INTRODUCTION

Bryophytes represent an ancient lineage of land plants and can be divided into three major groups: Marchantiophyta (liverworts), Bryophyta (mosses), and Anthocerotophyta (hornworts).^{1–3} In the past decade, *Marchantia polymorpha* has become a prevalent nonvascular plant model for studying evolutionary developmental biology questions including stem cell maintenance, cell fate determination and organ formation, hormone biosynthesis and perception, reproductive development, and evolution of life cycle strategies.^{4,5} As with other well-studied model plants, *M. polymorpha* offers several advantages to dissect gene function by a reverse genetics approach, such as high-quality genome sequence, short life cycle, low genetic redundancy, and easy transformation protocol.^{6–9}

M. polymorpha undergoes alternation of generations, with a multicellular haploid gametophyte generation alternating with a diploid sporophyte generation.^{2,10} As a typical bryophyte, gametophyte generation dominates the *M. polymorpha* life cycle. The haploid gametophyte begins with a unicellular spore that germinates and forms protonema, an initial short filamentous structure with rhizoids, through asymmetric cell division. The apical cell in the developing protonema subsequently gives rise to a complex plant body called the thallus. The thallus undergoes indeterminate planar growth with repeated dichotomous branching at

the apex,¹¹ resulting in a three-layered structure with visible dorsiventrality. The dorsal epidermis forms air chambers and gemma cups, whereas the ventral epidermis produces scales and rhizoids (see below for details). *M. polymorpha* can also reproduce asexually when the environmental conditions are favorable.^{12,13} The gemmae, the clonal propagules with two apical notches, are initiated on single-celled stalks at the bottom of gemma cups. After being released by raindrops, mature gemmae germinate and develop, producing clonal offspring.

Despite recent advances in understanding the regulatory mechanisms underlying the development of rhizoids, air chambers, gemma cups, and oil body cells in *M. polymorpha*,^{14–21} a comprehensive characterization of all cell types in gemmae and thalli has not been achieved. Moreover, how dormant gemmae quickly respond to moisture conditions during germination and how thalli undergo progressive maturation and senescence along with development are poorly understood. It is still unknown, however, if aging-related changes are evenly distributed in entire tissues or are limited to, arise in, or are driven by specific cell types in *M. polymorpha*.

The rapid development of single-cell RNA sequencing (scRNA-seq) technology provides exciting opportunities to systematically identify cell types and the entire cellular and molecular differentiation trajectory of plant stem cells.^{22–27} In this manuscript, we present the cell census of *M. polymorpha* across



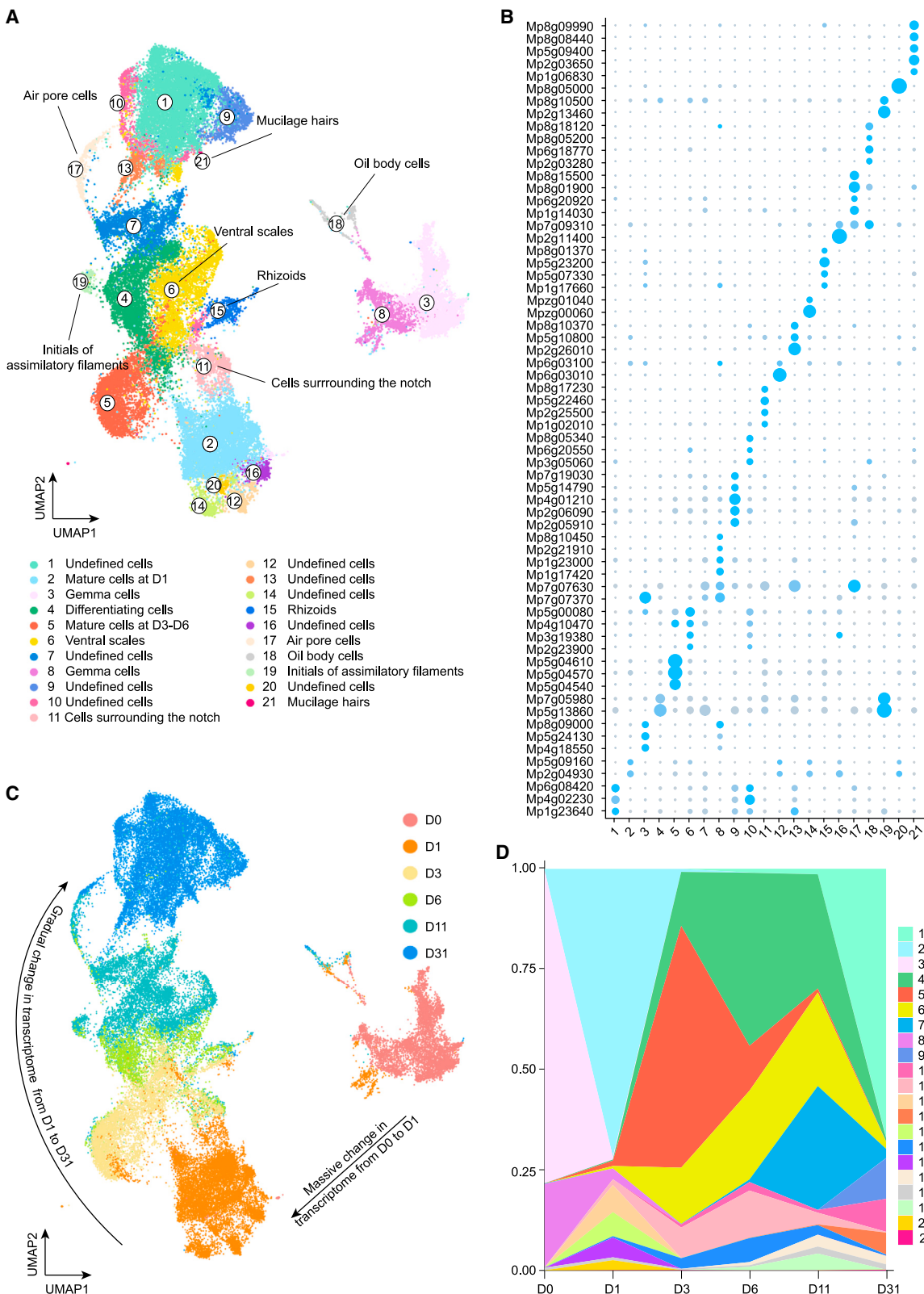


Figure 1. Generation of the *M. polymorpha* gemma and thallus cell census

(A) UMAP visualization of 21 cell clusters in *M. polymorpha* gemma (D0) and thallus from D1 to D31. Each dot denotes a single cell. Colors denote corresponding cell clusters. n = 46,136 cells.

(legend continued on next page)

asexual reproduction phases by profiling the transcriptomes of dormant gemmae and developing thalli of different stages at single-cell resolution. The cell types and gene signatures corresponding to oil body cells, air pore cells, rhizoids, ventral scales, initials of assimilatory filaments, mucilage hairs, and meristematic cells were identified. Moreover, time course comparisons at the cell-type level identified two progressive aging axes in the thallus. Remarkably, we found that the aging axis in the meristematic cells near the notch is temporally correlated with the formation of gemma cups, suggesting that the vigor of parent plants is determined by the number of offspring when resources are limited.

RESULTS

Generation of *M. polymorpha* gemma and thallus cell census

To generate a comprehensive cell census of male *M. polymorpha* (Takaragaike-1 [Tak-1]) across asexual reproduction phases, we chose dormant gemmae (hereafter referred to as the day 0 sample) and thalli spanning various developmental stages (1, 3, 6, 11, and 31 days after germination, hereafter referred to as the day 1, day 3, day 6, day 11, and day 31 samples, respectively) (Figure S1A). As previously reported,²⁸ rhizoids on the ventral epidermis were visible 1 day after transfer to culture medium. The thallus then grew radially with repeated dichotomous branching at the apex. At day 11, air chambers and gemma cups were formed on the dorsal surface of the thallus. The thalli became fully mature with massive production of gemmae at the bottom of the gemma cup at day 31.

The samples were harvested ($n = 2,000$ gemmae and thalli for the day 0 and day 1 samples, $n = 1,000$ thalli for the day 3 sample, 500 thalli for the day 6 sample, 50 thalli for the day 11 sample, and 5–6 thalli for the day 31 sample), digested into protoplasts (i.e., plant cells without a cell wall; Figures S1B and S1C), and subjected to scRNA-seq assays using the 10x Genomics Chromium platform separately. It should be noted that the protoplasting protocol for *Arabidopsis thaliana* did not work efficiently for *M. polymorpha*. We overcame this difficulty by increasing the enzyme concentration and adding Driselase (a cocktail of cell wall-degrading enzymes) in the digestion solution (see STAR Methods). We merged all the data and used standard computational pipelines in Seurat to align the raw sequencing data to the *M. polymorpha* genome and perform filtering, normalization, and integration.^{29,30} Approximately 44,600 reads were obtained per cell, which generated a median of 3,206 unique molecular identifiers (UMIs) per cell, 1,206 expressed genes per cell, and more than 15,600 total genes detected in the population (Table S1).

To mitigate the effect of protoplasting on the transcriptome, we performed bulk transcriptome sequencing (RNA-seq) before and after protoplasting for the day 31 thallus sample ($n = 2$).

Expression levels in the two biological replicates for each sample were highly correlated (Figure S1D). To identify differentially expressed genes (DEGs) in response to protoplasting, we compared gene expression levels between the pre- and post-protoplasting bulk RNA-seq datasets. We defined genes exhibiting consistent differential expression on protoplasting ($\log_2 [\text{fold change}] > 1$ or < -1) in both biological replicates as protoplasting-sensitive genes (Figure S1E; Table S1). Under this definition, 1,190 *M. polymorpha* protoplasting-induced genes were consequently excluded from downstream analyses. It should be noted that the removal of these genes did not affect cell clustering and topology of the cell census (Figure S1K). In addition, dead cells with high expression level of mitochondrial genes had no significant impact on downstream analysis (Figure S1L).

To further assess whether the resultant single-cell transcriptomes fully represent the loaded protoplast populations, we pseudo-bulked the transcriptomes of all captured cells. Gene expression levels in the pseudo-bulk were highly correlated with those in the bulk RNA-seq (Figure S1F), confirming that scRNA-seq captured a representative population of the gemmae and thalli cells.

After selecting highly variable genes, we used principal component analysis (PCA) on a gene expression matrix across 493 highly variable genes and identified 100 statistically significant principal components (PCs) ($p < 0.05$). We used Seurat to partition the 46,136 cells into 21 transcriptionally distinct clusters,³¹ which were further visualized on two-dimensional and three-dimensional uniform manifold approximation and projection (UMAP) plots (Figures 1A and S1G–S1J).^{32,33} By analyzing DEGs among the clusters, we identified a series of cluster-enriched or specific genes (Figure 1B; Table S1). Interestingly, the gemma cells (the day 0 sample) were separated from the thalli cells on the UMAP plot (Figures 1C and 1D), suggesting massive cell reprogramming at the transcriptome level during germination (i.e., from day 0 to day 1). By contrast, we observed a gradual change in transcriptomes in the samples from day 1 to day 31 (Figures 1C and 1D). Taken together, we generated a comprehensive cell census for the *M. polymorpha* gemma and thallus by time-resolved scRNA-seq.

Annotation of cell clusters of the *M. polymorpha* cell census

The thallus consists of a complex three-layered structure with distinct, differentiated cell types.⁴ The upper epidermal cell layer forms gemma cups and air chambers, which are equipped with air pores and assimilatory filaments. Although gemma cups are essential for asexual reproduction by forming gemmae from the bottom,¹² the air chamber facilitates gas exchange for photosynthesis and respiration.^{16,34} The middle region exerts a storage function by forming oil bodies, which contain a highly diverse mixture of sesquiterpenes and bisbibenzyls, in the subset of isolated cells referred to as idioblasts.^{18,20} The ventral

(B) Expression patterns of representative cluster-enriched genes. For each cluster, three genes are shown. Dot diameter represents the proportion of cluster cells expressing a given gene.

(C) Visualization of cell census by samples. The samples at different time points (from D0 to D31) are labeled with different colors. Two trajectories for transcriptome change are indicated.

(D) Temporal change of cell cluster compositions. Cluster names and colors are the same as in (A).

See also Figures S1.

epidermis is covered with rhizoids (unicellular tubular cells) and leaf-like scales.³⁵ Rhizoids develop from ventral epidermal cells or ventral scales by rapid tip growth and function in anchorage, nutrition assimilation, and water conduction.^{14,15,17,19,36} The ventral scales are usually arranged in three rows on each side of the thallus.⁴

Due to the scarcity of marker genes in *M. polymorpha*, the cell types of most cell clusters are unknown. We therefore used three strategies to *de novo* annotate cell clusters in the cell census. First, we surveyed genes whose biological functions or expression patterns have been well studied in *M. polymorpha*. Second, we generated promoter reporter lines for over 150 cluster-specific or enriched genes (Table S1). Third, we referred to *Arabidopsis* homologs of the cluster-specific or enriched genes (Table S1). Overall, these analyses enabled us to identify major differentiated cell types of gemmae and thalli. Notably, gene ontology (GO) analyses provided important insights into functionality of each cell type. Clusters 1, 7, 9, 10, 12, 13, 14, 15, and 20 could not be annotated because of the lack of cluster-specific genes (Table S1; see discussion below). We implemented a graphical user interface web server (<http://wanglab.sippe.ac.cn/Marchantia-census/>) to facilitate use of the datasets generated in this study. The spatiotemporal expression pattern of individual *M. polymorpha* genes can be queried in this web server.

Air pore cells

Cluster 17 radiated away from the central cell clusters (Figure 1A). GO analysis revealed that biological processes related to fatty acid and sterol biosynthesis were highly enriched (Figure S2G). The cluster-enriched genes *Mp5g06510* and *Mp4g19900* were exclusively expressed in the barrel cells of the air pore (Figures 2A and S2A; Table S1). Hence, cluster 17 was annotated as air pore cells of air chamber. Intriguingly, we also identified the gene signature for asymmetric cell division in this cluster, suggesting a common cell fate determination mechanism as stomata in higher plants.

Oil body cells (idioblasts)

Cluster 18 was topologically separated on the UMAP, indicating a unique physiological signature (Figure 1A). Interestingly, the oil body cell marker genes *MpERF13* (*Mp6g08690*), *MpABCG1* (*Mp8g13070*), and *MpSPY12B* (*Mp4g20670*) were highly expressed in this cluster (Figures S2H–S2J).^{18,20} Consistently, the expression of cluster-specific genes *Mp5g08940*, *MpMYB02* (*Mp3g07510*), and *Mp8g01220* were restricted to oil body cells in the thallus (Figures 2B, S2B, and S2C). GO analysis further revealed that biological processes related to the biosynthesis of terpenoids, isoprenoid, and aromatic constituents were overrepresented (Figure S2G). Moreover, farnesyl diphosphate synthase 1 (*FPS1*, *Mp3g22530*) and isopentenyl diphosphate isomerase 1 (*IPP1*, *Mp4g00610*), which play key roles in terpenoid and isoprenoid biosynthesis, were specifically expressed in this cluster (Figures S2K and S2L). Therefore, we annotated cluster 18 as oil body cells.

Rhizoids, ventral scales, initials of assimilatory filaments, and mucilage hairs

Cluster-15-specific gene *Mp2g14890* was exclusively expressed in rhizoids of the thallus (Figure 2C). Therefore, we termed cluster 15 as rhizoids. Cluster 6 was next to cluster 15 on the UMAP (Figure 1A). The promoter of cluster-6-specific gene *Mp6g16280* was predominantly active in scale cells on

the ventral side (Figure 2D). Thus, we identified cluster 6 as ventral scale cells. Gene signatures for transmembrane transport and response to nutrition level were overrepresented in this cluster (Figure S2G), suggesting a potential role of the ventral scale in assimilation.

Based on reporter gene expression patterns, we further assigned clusters 19 and 21 as initials of assimilatory filaments and mucilage hairs, respectively: Cluster 19-specific gene *Mp2g13460*, which encodes a chlorophyll a/b binding protein, was highly expressed in the initials of assimilatory filaments at the bottom of the air chamber (Figure 2E), whereas promoter activity of the cluster-21-specific gene *Mp5g09850* was only detected in mucilage hairs covering the notch on the ventral side (Figure 2F). Consistent with a supportive role in gas exchange for photosynthesis in the air chamber,⁴ cluster 19 was enriched in genes related to photosynthesis (Figure S2G).

Meristematic cells surrounding the notch

Cluster 11 was highly enriched in genes related to DNA replication, cell cycle, and chromatin modifications (Figure S2G; Table S1). For instance, *MpHMGBOX2* (3xHigh Mobility Group-box2, *Mp2g12330*), *histone H3* (*Mp7g10730*), *histone H4* (*Mp5g22460*), *Cyclin A1;1* (*CYCA1;1*, *Mp2g25500*), and *cyclin-dependent kinase B1;2* (*Mp5g19170*) were significantly enriched (Figures S2M–S2Q). Promoter reporter analyses further revealed that the cluster-specific genes *Mp1g28360*, *Mp3g15450*, *Mp5g10030*, and *Mp1g19500* were highly expressed in cells near the notch (Figures 2G and S2D–S2F). Thus, we identified cluster 11 as the meristematic cells surrounding the notch.

Mature somatic cells

The cells in cluster 2 mainly belonged to the day 1 sample (Figure S1I). One of the cluster-enriched genes, *Mp5g09160*, was preferentially expressed in the mature and differentiated cells in the middle of the day 1 thallus (Figure 2H). Similarly, cluster 5 was designated as the mature somatic cells in the day 3 and day 6 thalli (Figures 2I and S1I). Consistently, we found that ribosomal protein and photosynthesis genes such as *RIBOSOMAL PROTEIN L12* (*RPL12*, *Mp5g15720*), *RPL15* (*Mp1g23700*), and *photosystem II reaction center protein A* (*Mp5g10950*) were highly enriched in these two clusters (Figures S2R–S2T; Table S1).

Differentiating cells

Cluster 4-enriched gene *Mp7g04610* was mainly expressed in cells between the notch cells and mature somatic cells (Figure 2J). Biological processes related to photosynthesis and ribosomal RNA processing were overrepresented in these cells (Figure S2G). Thus, cluster 4 represented differentiating thallus cells, analogous to the transit-amplifying cells in the shoot apical meristem in *Arabidopsis*.³⁷

The collection of cell-type-specific genes accelerates gene discovery

Previous results have shown the power of scRNA-seq technology in acceleration of gene discovery in *Arabidopsis*, maize, and rice.^{37–40} We attempted to ask whether the cell-cluster-specific gene list, combined with genome editing tools such as CRISPR-Cas9, could also help us uncover new cell-type-specific regulators in *M. polymorpha* with high accuracy.

As a proof of concept, we first focused on cluster 17 (air pore cells). We identified *MpHSF1* (*Mp4g12230*), which encodes a

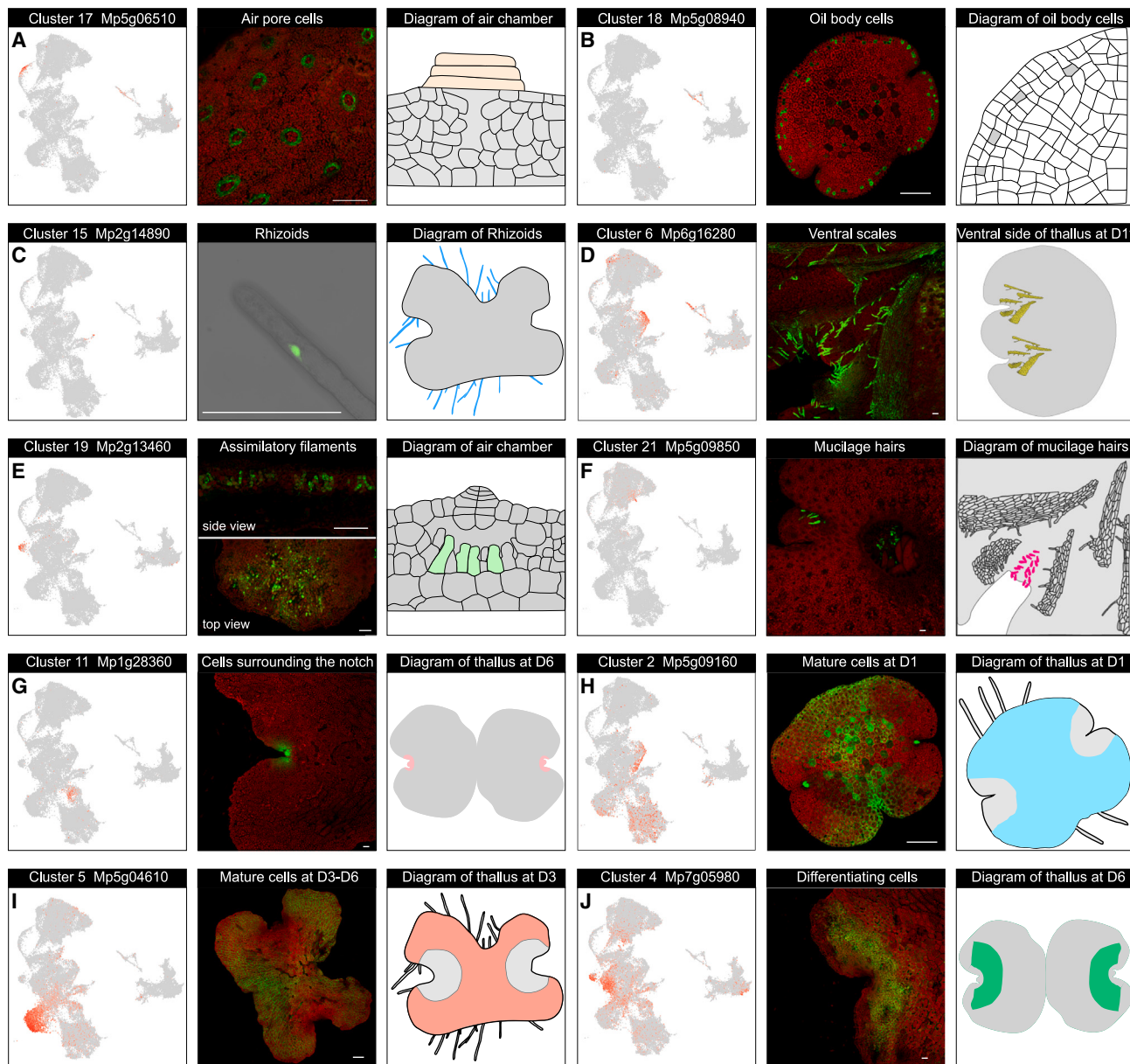


Figure 2. Annotation of cell clusters and expression of marker genes

Ten cell clusters are shown. For each (A)–(J), the expression pattern of the representative gene on the UMAP (left), the Citrine promoter reporter (green) expression pattern *in planta* (middle), and a schematic of the expression pattern (right) are shown. Red, autofluorescence of chloroplasts. One representative image for each reporter is shown. To better visualize the expression pattern in rhizoids (C), we used nuclei-localized Citrine as a reporter (see STAR Methods). Scale bars, 200 μ m.

See also Figures S2.

heat shock factor specifically expressed in this cluster (Figure 3A). To generate null alleles by CRISPR-Cas9 technology, we created the *MpHSF1* mutant designing two single-guide RNAs (sgRNAs) within the coding region (Figure S3A). Three independent alleles with the same phenotype were obtained. Compared with wild type, the number of air pores on the dorsal epidermis of the *MpHSF1* mutant was greatly reduced as revealed by scanning electron microscope (SEM) analysis (Figures 3B–3D), suggesting that *MpHSF1* plays an important role in specification of barrel cells of air pore.

We then generated the loss-of-function mutant of *MpMYB02*, which is exclusively expressed in oil body cells (cluster 18, Figures 3E and S3B).²⁰ Interestingly, Nile Red staining and bright-field microscopic examination revealed that the oil body cells of the mutant are largely intact but devoid of oil bodies at day 0 and day 3 (Figures 3F–3H). The oil body cells were distinguishable from surrounding cells due to less differentiated chloroplasts (Figures 3G and 3H). Thus, these results are consistent with previous findings that *MpMYB02* regulates cyclic bis(benzyl) acids biosynthesis⁴¹ and acts downstream of *MpERF13*, a

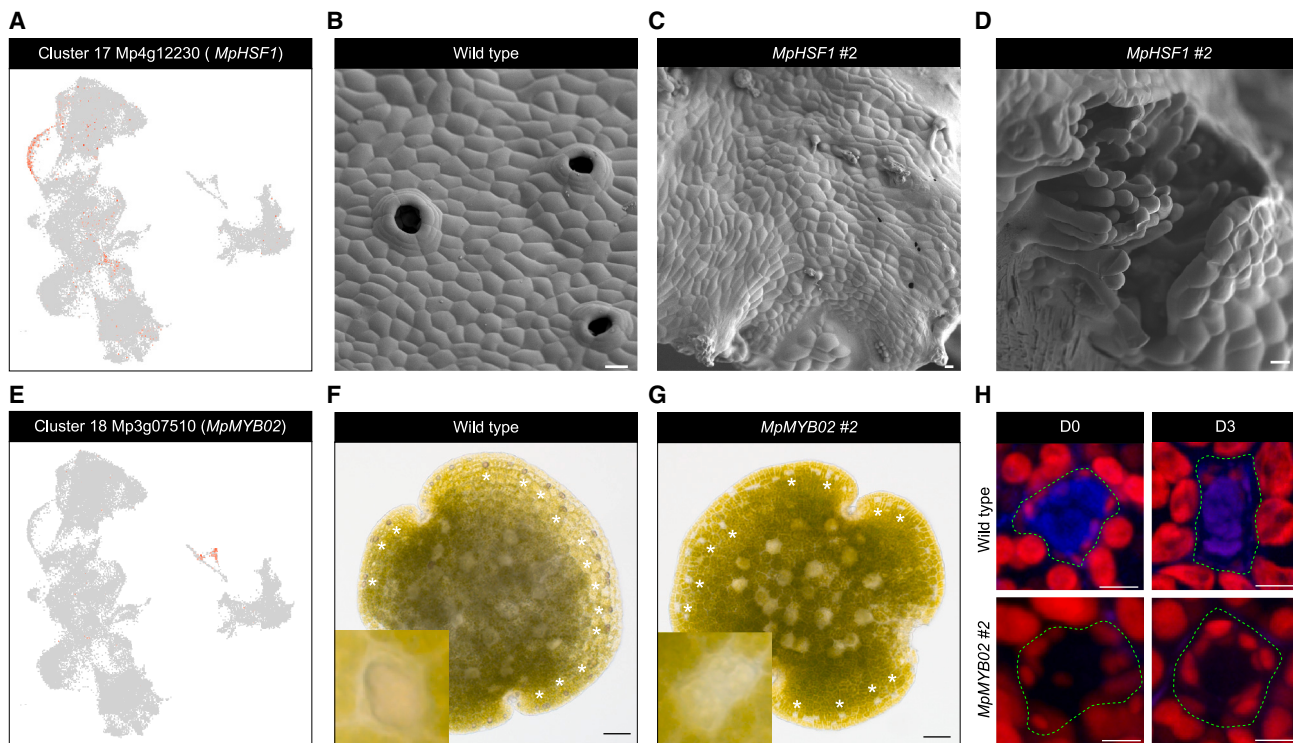


Figure 3. Gene discovery based on cluster-specific genes in *M. polymorpha*

(A) UMAP showing the expression pattern of *MpHSF1*.

(B–D) SEM imaging of the dorsal epidermis of wild-type (B) and *MpHSF1* mutant (#2) (C and D). Please note that mutants were largely devoid of air chambers (C). Occasionally, they developed air pores with strong defects in barrel cells (D).

(E) UMAP showing the expression pattern of *MpMYB02*.

(F and G) Representative images of the gemmae and oil body cells (insets) in wild-type (F) and *MpMYB02* mutant (#2) (G) at day 0. White asterisks indicate oil body cells.

(H) Visualization of oil body (blue) by Nile red staining at day 0 and day 3. Red, autofluorescence of chloroplasts. The oil body cells are outlined by green dashed lines. Please note that the oil body cells in the mutant did harbor chloroplasts. Scale bars: 20 μ m in (B)–(D); 100 μ m in (F) and (G); and 5 μ m in (H).

See also Figure S3.

master regulator of oil body formation.²⁰ Importantly, the mutant phenotype further implies that *MpMYB02* does not contribute to the commitment of oil body cell fate. Taken together, above results indicate that the cell census generated in this study can serve as a valuable resource for *M. polymorpha* functional genomics in the future.

Massive cell reprogramming at the transcriptome level during germination

The most striking feature of our *M. polymorpha* cell census is that the thalli at different developmental stages harbor distinct transcriptome signatures (Figure 1C). Most gemmae localized in clusters 3, 8, and 18 and were separated from the thalli cells (Figures 1A, S4A, and S4B). This pattern indicates that, although mature gemmae are anatomically organized and composed of different cell types, all cells, except oil body cells, are similar at the transcriptome level. GO analysis further revealed that defense response genes were overrepresented in cluster 8, whereas cluster 3 cells showed gene signatures for seed dormancy and germination (Figure S2G). It is highly possible that cluster 3 represents some gemmae undergoing germination in response to moisture conditions during proto-

plasting. Consistent with the role of abscisic acid (ABA) in gemma dormancy,^{28,42} the expression levels of ABA-related genes were greatly reduced during germination (Figures S4C and S4D).

A progressive aging axis along the midvein of the *M. polymorpha* thallus

Thallus cells at the same time point tended to group together on the UMAP (Figures 1C and 4A), suggesting a gradual change of transcriptomes along with thallus maturation and aging. To evaluate this hypothesis, we used Scissor, a newly developed scRNA-seq algorithm based on Pearson's correlation coefficient and regression model.⁴³ We used thallus developmental age to guide Scissor analysis. Cells with non-zero regression coefficients were assigned as Scissor positive (Scissor⁺, red dots) cells and Scissor negative (Scissor⁻, blue dots) cells, which are positively and negatively associated with maturation and aging, respectively (Figure 4B). Cells with coefficients of zero were indicated as background cells (gray dots in Figure 4B). As anticipated, the proportion of Scissor⁺ cells increased along with the developmental time of the samples (Figure 4B). Notably, most of the day 31 cells were assigned as Scissor⁺ cells. Consistent with

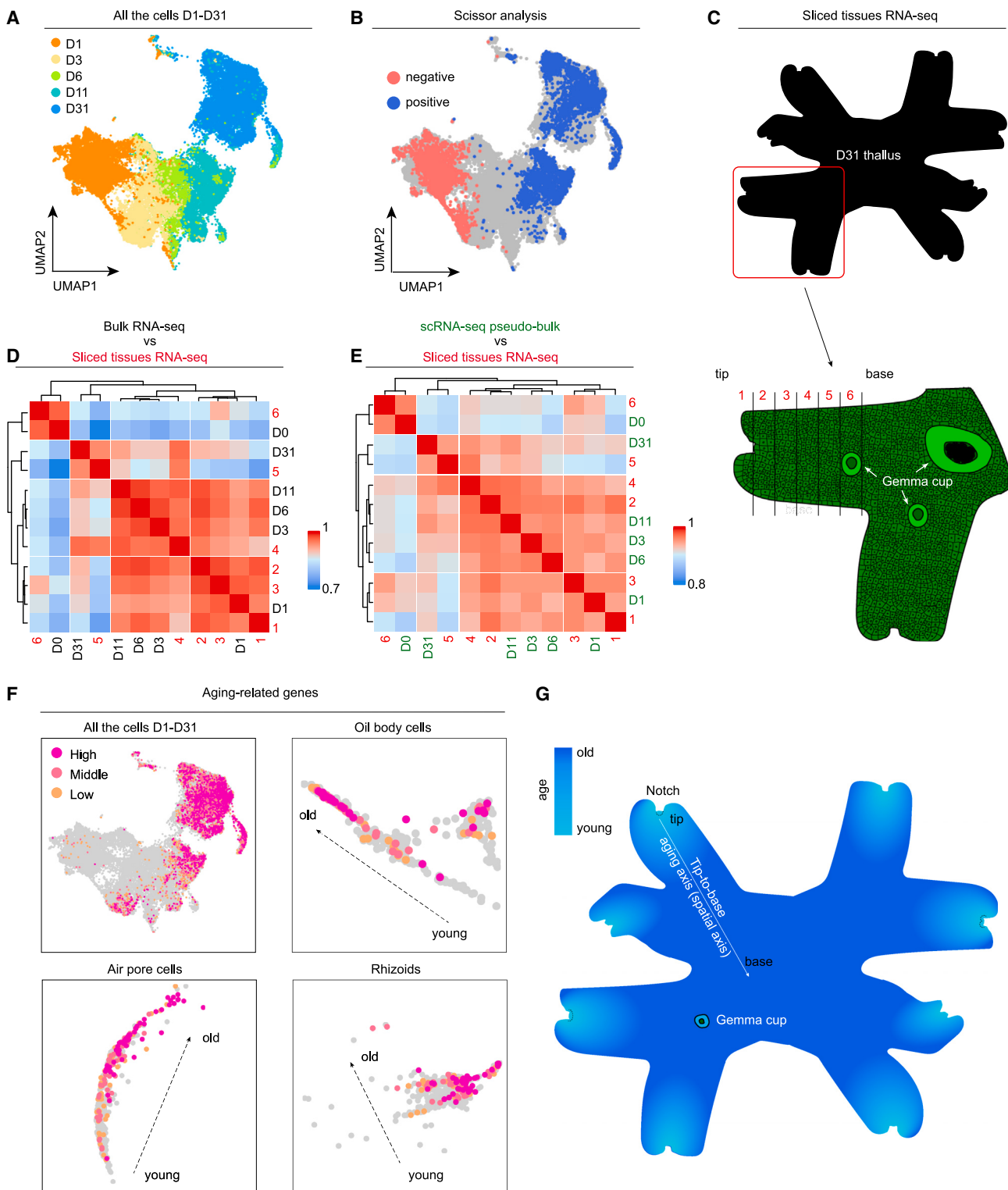


Figure 4. The tip-to-base maturation and aging axis along the midvein

(A) UMAP plot showing the thallus cell census colored by different time points (from D1 to D31). Color code is the same as in Figure 1C. n = 40,223 cells.

(B) Scissor analysis. UMAP plot showing the cells positively (blue dots) and negatively (red dots) correlated with aging. The UMAP is same as in (A).

(C) Schematic of the sliced tissues RNA-seq experiment. The 31-day-old thallus was chopped into six slices (1–6 respectively). Each slice was subjected to RNA-seq. Three biological replicates were performed. Please note that slice #6 harbored the gemma cup (light green).

this finding, aging-related genes were highly enriched in the day 31 cells (Figure 4F).

Each thallus contains a wide range of tissue ages, from the young, actively growing tip regions to the older, mature basal parts, suggesting that the observed progressive aging revealed by scRNA-seq may actually reflect the tip-to-basal aging axis in the thallus. To confirm this hypothesis, we performed spatially resolved RNA sequencing on the thallus. We sliced the 31-day-old thallus from tip-to-base into six slices (Figure 4C). The resultant sliced tissues RNA-seq data were compared with the bulked RNA-seq and pseudo-bulked scRNA-seq transcriptomes at different time points. As shown in Figures 4D and 4E, slices 1–3, 4, and 5 aligned with the bulk and pseudo-bulked samples of day 1, days 3–11, and day 31, respectively. Interestingly, slice 6, which harbored gemma cups (Figure 4C), was highly correlated with the gemmae samples (Figures 4D and 4E). These results collectively indicate a progressive aging axis (i.e., spatial aging axis) along the midvein of the thallus (Figure 4G).

The maturation and aging trajectory of oil body cells

We next investigated the maturation and aging of specialized cell types of the thallus at single-cell resolution. We first delineated the maturation and aging trajectory of oil body cells. As shown in Figure 5A, the oil body cells (cluster 18) were arranged in a stretched trajectory pattern. In particular, the oil body cells of the early samples (i.e., the day 0 and day 1 thalli) were gathered on one side of the trajectory, whereas those of the late sample (i.e., the day 31 thallus) were scattered (Figure 5A). Because the late sample harbored the oil body cells across all developmental stages, these results indicate a spatial (tip-to-base) maturation and aging axis of the oil body cells in the thallus. In agreement with this conclusion, aging-related genes were highly expressed in the day 31 oil body cells (Figure 4F). A similar pattern was observed in the air pore cells (cluster 17), rhizoids (cluster 15), and ventral scales (cluster 6) (Figures 4F and 5B–5D).

We then re-clustered all oil body cells. As shown in Figure 6A, cluster 18 could be grouped into four distinct sub-cell clusters (O1–O4). As expected, all sub-cell clusters were enriched in biological processes related to isoprenoid and terpenoid biosynthesis (Figure 6B). Genes involved in RNA splicing, protein processing, seed germination, and seedling development were overrepresented in the cells in clusters O1 and O4. By contrast, cluster O2 showed a gene signature for aging (Figure 6B). Intriguingly, the old oil body cells (i.e., cluster O2 cells) were also enriched in the genes related to photosynthesis. Consistent with the results in Figure 5A, the day 31 oil body cells mainly resided in cluster O2 but were also presented in other sub-cell clusters (Figure 6C). Thus, these results collectively imply that young oil body cells in the tip region are mainly involved in defense against arthropod herbivores by producing high amounts of specialized metabolites. Along with the tip-to-base maturation

axis, old oil body cells gradually adopt a metabolic state directed to carbohydrate biosynthesis, thereby sustaining normal thallus growth (Figure 6D).

In agreement with this hypothesis, the total plan area of chloroplasts in the base region was higher than in the tip region in the day 31 thalli (Figures 6E–6H), probably due to an increase in plan area of the individual chloroplast (Figure 6E). In addition, we could observe grana (stacked thylakoids) in the chloroplasts of oil body cells in the base (Figure S5), as revealed by transmission electron microscope (TEM) analysis. Furthermore, expression of the genes involved in terpenoid and isoprenoid biosynthesis such as *FPS1*, *IPPI*, *ISPF* (*Mp1g29200*), and *GGPS* (*Mp2g13280*) were greatly reduced in cluster O2, accompanied by increased levels of photosynthesis-related genes (Figures 6I–6K). Taken together, our scRNA-seq analysis uncovered a previously unrecognized maturation and aging trajectory of the oil body cells.

A temporal maturation and aging trajectory of meristematic cells near the notch

In addition to specialized cell types, we noticed that the meristematic cells near the notch (cluster 11) also exhibited a similar transcriptome change with age (Figure 5E). Because these cells consistently localize in the notch or the tip region of each branch during the thallus development, this result indicates that the maturation and aging trajectory of these cell populations is directed by a temporal rather than a spatial cue (i.e., temporal aging axis in Figure 7M, see below). Consistently, each sub-cell cluster of the meristematic cells near the notch (N1–N4) was composed of cells from different time points (Figures 7A–7C).

Meristematic activity is positively correlated with cell division rates in plants. We therefore investigated cell division frequency in the notch at different developmental stages by examining expression of the miotic reporter (*CYCA1;1::Citrine*), in which *Citrine* was expressed from the regulatory sequence of *CyclinA1;1* (*Mp2g25500*), a key cell-cycle progression factor. As shown in Figure 7D, we observed high reporter activity in cells near the notch from day 1 to day 6. Citrine fluorescence dropped at day 11 when the gemma cup began to form.

The inflorescence meristem of monocarpic plants usually arrests after production of a certain number of fruits. Such a strategy is recognized as a way to optimize allocation of resources to the production of seeds and hence reproductive success.^{44–46} In *Arabidopsis*, the removal of siliques or sterility prevents inflorescence arrest at the reproductive stage,⁴⁵ suggesting that an unknown signal produced by developing seeds is a trigger for inflorescence meristem arrest.^{45,47,48} Considering the similarity of this process with the progressively decreased meristematic activity with age in *M. polymorpha*, we speculated that formation of the gemma cup (i.e., the onset of asexual reproduction) could affect the maturation and aging of the meristematic cells near the notch in parent plants.

(D and E) Correlation analysis between sliced tissues RNA-seq and RNA-seq samples. The sliced tissues RNA-seq samples are labeled in red, whereas the bulk RNA-seq (D) and pseudo-bulk scRNA-seq (E) samples are in black and green respectively.

(F) Expression of aging-related genes. The expression levels were sorted into three categories: high, middle, and low. The UMAP is same as in (A) for all cells from D1 to D31, and in (A)–(C) for oil body cells, air pore cells, and rhizoids. Dashed arrows, maturation and aging trajectory for each cell type.

(G) Schematic of the maturation and aging trajectory of the main plant body of *M. polymorpha* along the tip-to-base axis of the midvein.

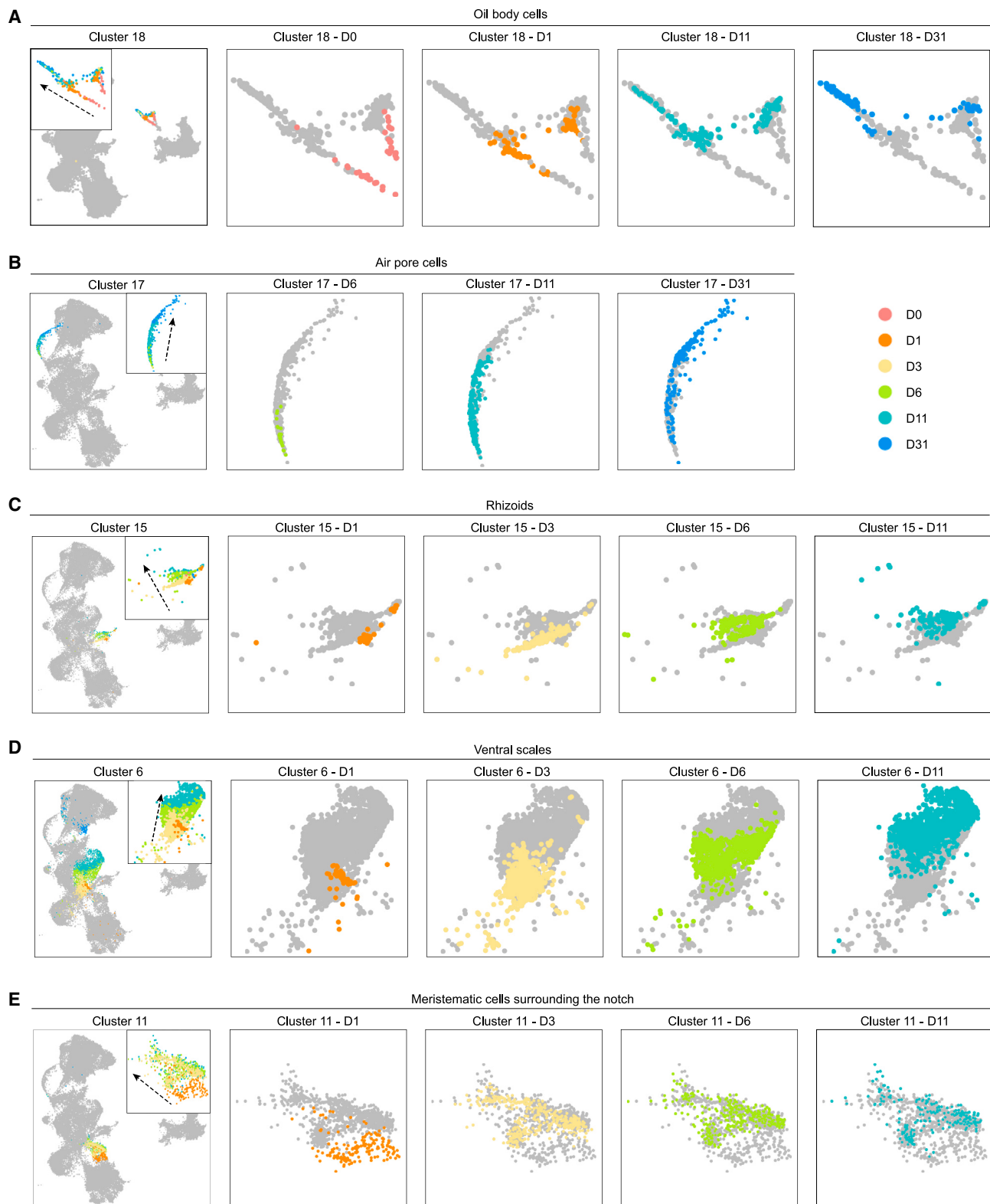


Figure 5. Cell-type maturation and aging trajectory at single-cell resolution

Five cell types (A–E) are shown. UMAP plots were colored by different time points (D0, D1, D3, D6, D11, and D31). The color code is the same as in Figure 1C. Dashed arrows, maturation and aging trajectory for each cell type.

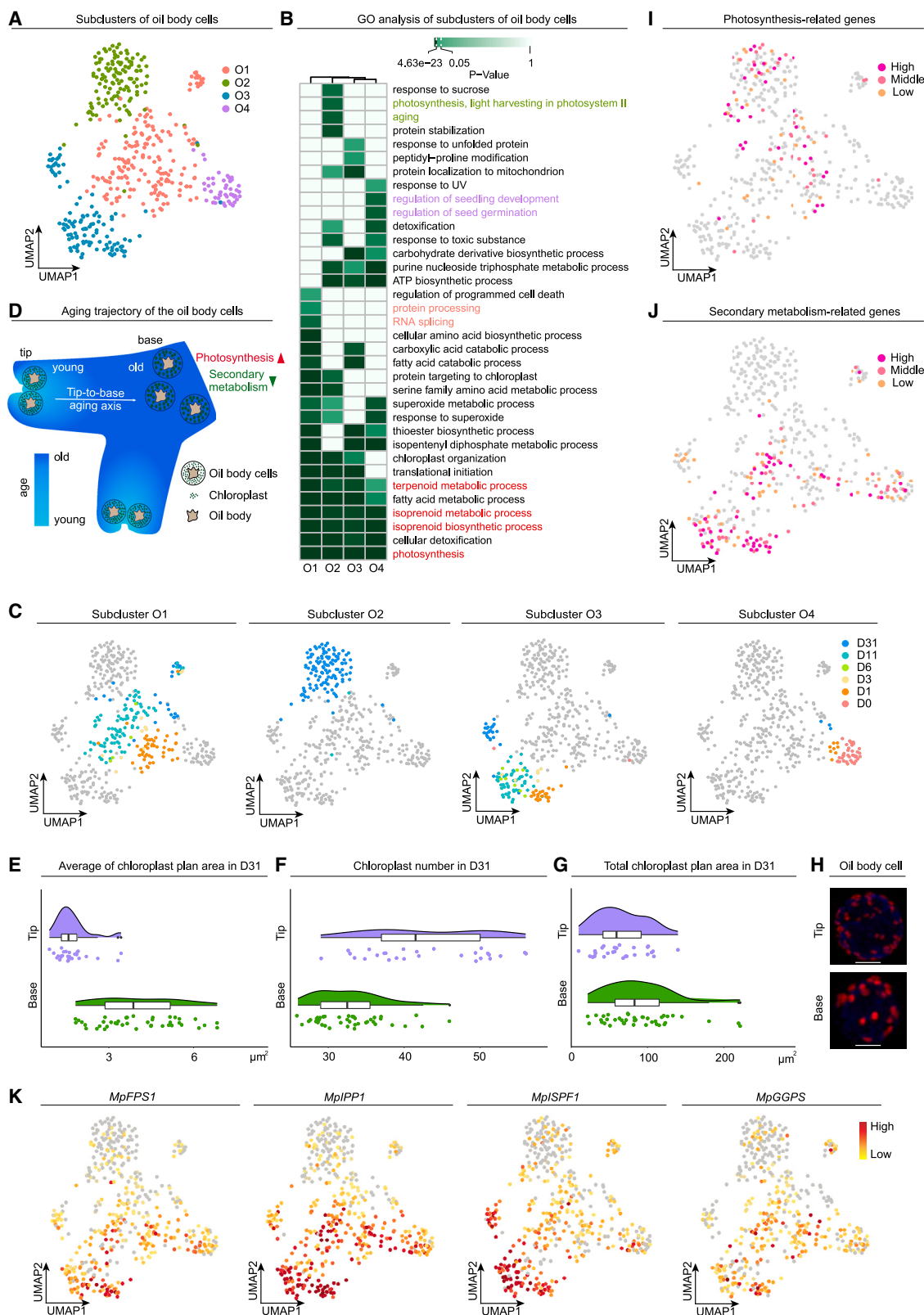


Figure 6. Maturation and aging trajectory of oil body cells

(A) Sub-cell clustering of cluster 18 (oil body cells). Four sub-cell clusters (O1–O4) are shown. n = 460 cells.

(B) GO term analysis. The differentially enriched GO terms are highlighted in different colors. p values are given on the top.

(legend continued on next page)

To test this hypothesis, we first grew the thalli for 14 days and then manually removed gemma cups under a stereomicroscope. The growth rates of samples with gemma cups removed and intact thalli were recorded from day 0 to day 6. As expected, removal of the gemma cups resulted in accelerated growth of the thalli (Figures 7F, 7G, and S6A), particularly from day 0 to day 4 (Figure S6B). To rule out differences between individual thalli, we further cut a single thallus into two equivalent halves from the middle. One half was used as a control and the other half was subjected to the same gemma cup removal experiment (Figure 7E). Similar to the results described above, the samples depleted of the gemma cups grew faster than intact samples (Figure 7I). These results indicate a trade-off between asexual reproduction and thallus growth rate.

To compare cell division rates between samples with gemma cups removed and intact samples, we examined expression of the CYCA1;1::Citrine reporter. Consistent with an increase in growth rate, the reporter activity was significantly elevated near the notch in the samples with gemma cups removed (Figures 7J and 7K). Moreover, cell area measurement revealed that the accelerated growth of the thalli was not due to an enlargement of epidermal cells (Figure 7L). Thus, the above results identify a maturation and aging trajectory of meristematic cells near the notch (Figure 7M). Notably, the decreased meristem activity is temporally correlated with formation of the gemma cups, suggesting an ancient strategy to optimize allocation of resources to the production of offspring. The vigor of parent plants is therefore determined by the number of offspring when resources are limited.

Taken together, by profiling the transcriptomes of thalli at single-cell resolution, we have uncovered two maturation and aging axes of the main plant body of *M. polymorpha* (Figure 7M): the gradual maturation of tissues and organs along the spatial axis (tip-to-base) and the progressive decline of meristem activities in cells near the notch along the temporal axis (e.g., from day 1 to day 31). The cell census and continuous developmental trajectories for each cell types lay the groundwork for fully understanding the maturation program of *M. polymorpha* thallus in the future.

DISCUSSION

Bryophytes represents a sister to the rest of land plants.² Despite their evolutionary importance and relatively simple body plan,⁴ a comprehensive understanding of the cell types and transcriptional states that underpin their temporal development and aging has not been achieved. Here, we addressed this challenge by

identifying molecular cell types of *M. polymorpha* gemmae and thalli using time-resolved scRNA-seq. The resulting cell census provides a platform for investigations into the developmental principles of *M. polymorpha*, as well as other bryophytes.

The number of cell types changes during evolution. In general, cell-type number can be used as an index of morphological complexity. For instance, relatively few cell types have been identified in basal metazoans,⁴⁹ suggesting a massive expansion of cell-type diversity before the origin of bilaterians.⁵⁰ In line with this observation, we found that the *M. polymorpha* gemmae and thalli have fewer cell types than the vegetative shoot and root apices of *Arabidopsis* (Figure S7A).^{37,51-57} In particular, the degree of cell heterogeneity among different cell clusters is low in *M. polymorpha* as fewer cluster-specific genes have been identified and validated (Figures S7A–S7D; Table S1).

We could only obtain cluster-enriched genes for clusters 1, 7, 9, 10, 12, 13, and 20. The reporters based on these genes did not yield specific expression patterns (Table S1). As a consequence, the identities of these seven clusters remain unclear at current stage. Importantly, we failed to identify the clusters related to epidermis and parenchymatous storage cells, suggesting that *M. polymorpha* epidermis is less differentiated than that in *Arabidopsis* and thereby not separable from parenchymatous storage cells at the transcriptome level. Indeed, we could not identify a single and specific cluster based on the dorsal epidermis marker genes *MpC4HDZ* (*Mp7g09710*) and *MpSBG9* (*Mp1g09420*) (Figures S7E and S7F).^{58,59}

The specific cluster related to gemma cups has not been assigned as well. *GEMMA-CUP-ASSOCIATED MYB1* (*GCAM1*, *Mp6g04830*), which is essential for gemma cup initiation,²¹ is weakly expressed (Figure S7G). By contrast, *KARAPPO* (*KAR*, *Mp5g06550*), a gene required for the specification of gemma initial cells,⁶⁰ shows a broad expression pattern in the census (Figure S7H). Hence, it is likely that gemma cup cells are transcriptomically similar to epidermal cells, whereas the floor cells are not efficiently captured due to a low cell proportion in thalli.

It should be noted that cell types could also have been lost during evolution. For instance, cone receptor types were lost in response to a nocturnal lifestyle in early mammals.⁶¹ Similarly, the cell types associated with leaf and root development have degenerated in the parasitic plant *Cuscuta australis*.⁶² Therefore, it remains unclear whether all *M. polymorpha* cell types identified here can be found in other bryophytes. It is highly possible that certain cell types of gemmae and thalli are only specific for liverwort. For example, the existence of oil body cells is unique to liverworts and can be considered as a synapomorphy of this lineage.^{20,63} Thus, elucidating the identities and functions of all cell

(C) UMAP plots showing sub-cluster cells colored by different time points (D1–D31). Color code is the same as in Figure 1C. The UMAP is same as in (A).

(D) Schematic of the maturation and aging trajectory of the oil body cells along the tip-to-base axis of the midvein. Young oil body cells in the tip region produced high amounts of specialized metabolites, whereas old oil body cells in the base region adopted a metabolic state directed to photosynthesis. Two branches of a thallus are shown.

(E–G) Quantification of chloroplasts in the oil body cells in 31-day-old thalli. The oil body cells at the tip or base region of 31-day-old thalli were harvested. The average blade area (E), number (F), and total chloroplast plan area (G) were quantified. n = 28 (tip) and 40 (base) oil body cells. Data are presented as raincloud plots showing the median (black line) and interquartile range (box).

(H) Representative images of the oil body cells at the tip or base region of 31-day-old thalli. Blue, oil body as revealed by Nile red staining. Red, autofluorescence of chloroplasts. Scale bars, 20 μ m.

(I and J) Expression of photosynthesis (I) and secondary metabolism-related (J) genes. The UMAP is the same as in (A).

(K) UMAP plots showing the selected secondary metabolism-related genes. The UMAP is the same as in (A).

See also Figure S5.

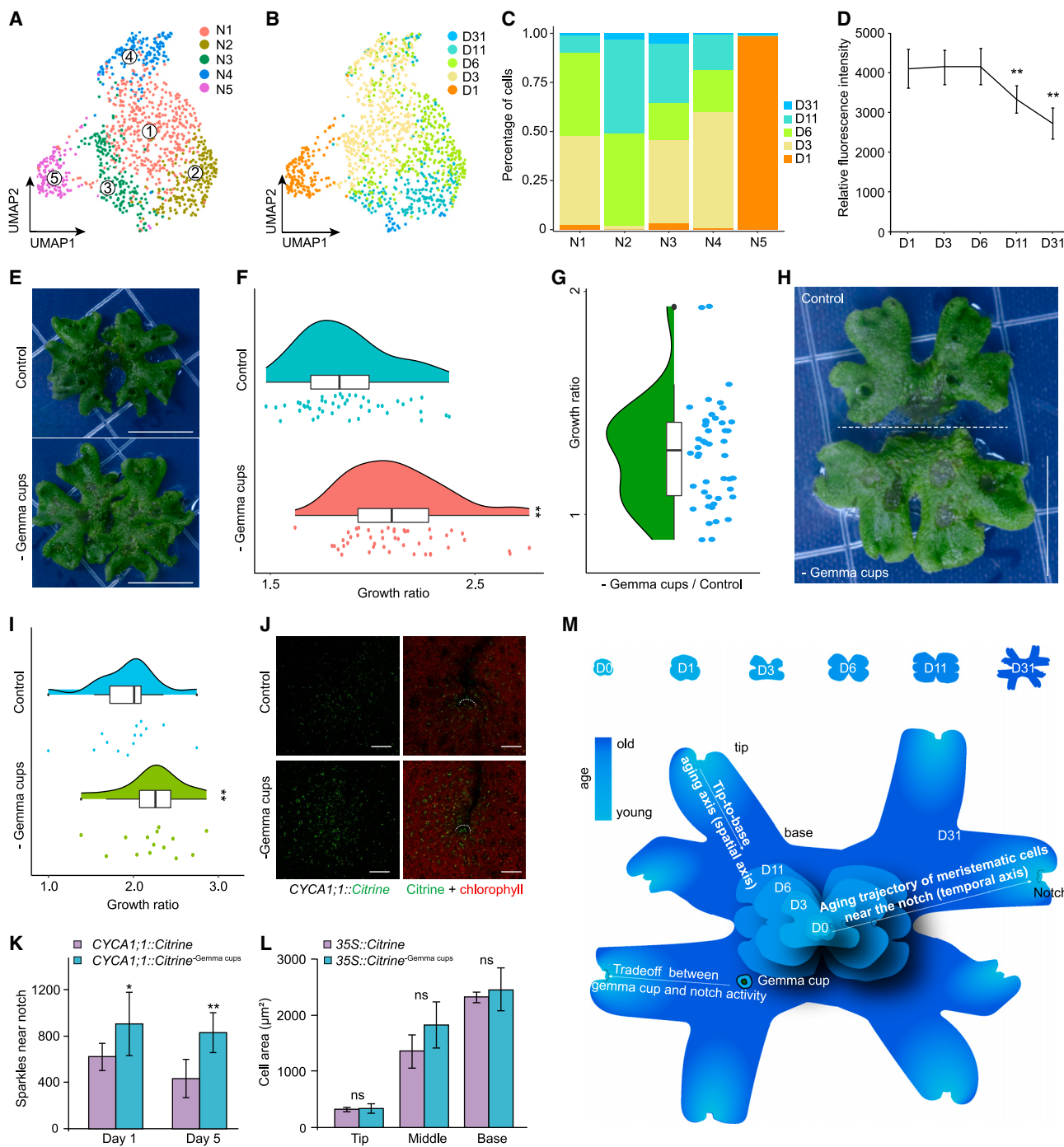


Figure 7. Progressive decline of meristem activities in the tip along a chronological axis

(A) Sub-cell clustering of cluster 11 (cells surrounding the notch). Five sub-cell clusters (N1–N5) are shown. n = 1,168 cells.

(B) UMAP plot showing cluster 11 colored for different time points (D1–D31). The color code is the same as in Figure 1C. The UMAP is same as in (A).

(C) Proportions of cells at different developmental stages (D1–D31) at each sub-cell clusters. The color code is the same as in Figure 1C.

(D) The expression level of the CYCA1;1::Citrine reporter near the notch at different developmental stages (D1–D31). **p < 0.01, two-tailed, Student's t test.

(E) Plant phenotype. One representative control (top) and plant with gemma cups removed (bottom) are shown. Photos were taken 6 days after gemma cup removal. Scale bars, 1 cm.

(F) Quantification of the growth ratio in control and samples with gemma cups removed. For the control experiment, n = 40 thalli; for gemma cup removal experiments, n = 40 thalli. Data are presented as a raincloud plot showing values of each sample (dots), the median (black line) and interquartile range (box).

**p < 0.01, two-tailed, Student's t test.

(G) Relative growth ratio between control and plants with gemma cups removed based on the results in (F).

(legend continued on next page)

types in *M. polymorpha* will boost our understanding of the developmental trajectory of the main body of many bryophytes in the future.

It is currently unknown how production of the gemma cup affects meristem activities. In *Arabidopsis*, it has been proposed that inflorescence meristem arrest was triggered by fruits, probably via energy depletion or an unknown death hormone derived from developing seeds.^{45,47,48} Recently genetic studies have shown that the MADS-box transcription factor FRUITFULL (FUL) promotes meristem arrest through repressing microRNA172-targeted *APETALA2* (AP2)-like genes.⁶⁴ The decreased level of these genes results in an impairment of *WUSCHEL* (*WUS*) expression and reduced proliferative capacity in the meristem. In addition to the FUL-AP2-WUS pathway, the plant hormones auxin and cytokinin have been implicated in inflorescence meristem arrest. The arrest of each inflorescence is proposed to be a local process, driven by auxin export from fruit proximal to the inflorescence apex.⁶⁵ Cytokinin signaling repression, by contrast, contributes to proliferative arrest of inflorescences at the end of the *Arabidopsis* flowering period.^{66,67} Therefore, it is important to unravel whether auxin and cytokinin are also involved in the proliferative slowing down in the *M. polymorpha* notch and, if true, whether this altered hormone response is triggered by the formation of the gemma cup. Certainly, another important research direction is identifying the mobile signal and specific cell types underlying this long-distance communication.

Cell types are building blocks of multicellular organisms that exhibit extensive diversity.⁶⁸ From an evolutionary perspective, cell-type identity is defined by the regulatory mechanisms that enable and maintain the distinct gene expression profile of a cell type within the organism.⁶⁹ As such, cell types can be considered as evolutionary units with the potential for independent evolutionary change. Recently, the advent of scRNA-seq has facilitated cross-species comparisons of cell types in animals.^{70–72} For example, comparisons among invertebrate and vertebrate cell censuses identified muscle cells and neurons as conserved cell types and inferred cross-species transcription factor regulatory programs underlying cell-type identity.^{71,73} Therefore, future generation of high-resolution organism-wide plant cell censuses by large-scale scRNA-seq across bryophytes, lycopophytes, ferns, and gymnosperms will lead to the discovery of previously unrec-

ognized cell types and provide an unprecedented opportunity for systematic comparative analysis of cell types across diverse plant species.^{22,74,75} Particularly, whether shared gene expression patterns can lead to identify unexpected evolutionary homologies is an interesting and important research topic.

We anticipate that the construction of a cross-species organism-level cell-type evolutionary tree will shed light on the origins and evolutionary hierarchies of major plant cell types, uncover the gene regulatory network underlying cell-type innovation and ultimately delineate the evolutionary trajectories along land plant diversification at cell-type resolution.

Limitations of the study

Our study has two main limitations. First, the cell census of *M. polymorpha* across asexual reproduction phases remains incomplete. Because we sampled the whole thalli for scRNA-seq, the proportion of cells near the notch was relatively low. In the future, profiling these cells specifically at single-cell resolution will be necessary to identify cells in the apical meristem and unveil how stem cells progressively differentiate into various cell types. Second, we were unable to annotate several cell clusters due to the lack of cluster-specific genes. Therefore, applying spatial transcriptomics will aid us in mapping the location of these cell clusters within the thallus in the future.

STAR★METHODS

Detailed methods are provided in the online version of this paper and include the following:

- KEY RESOURCES TABLE
- RESOURCE AVAILABILITY
 - Lead contact
 - Materials availability
 - Data and code availability
- EXPERIMENTAL MODEL AND SUBJECT DETAILS
- METHOD DETAILS
 - Constructs
 - Generation of transgenic plants
 - Microscope
 - Sliced tissues RNA-seq and bulk RNA-seq

(H) Plant phenotype. The plants were cut into two halves (dashed line). One was used as control, whereas the other half was used for gemma cup removal experiments. Photos were taken 6 days after gemma cup removal. Scale bars, 1 cm.

(I) Quantification of the growth ratio in control and samples with gemma cups removed as described in (H). **p < 0.01, two-tailed, Student's t test.

(J) Expression pattern of the CYCA1;1::*Citrine* reporter near the notch (dashed line). Scale bars, 100 μm.

(K) Quantification of cell division activities as revealed by expression of the CYCA1;1::*Citrine* reporter. The number of Citrine-positive cells near the notch were counted. n = 5 thalli. *p < 0.05, **p < 0.01, two-tailed, Student's t test.

(L) Quantification of the cell area. In order to visualize the cell outlines precisely, we used the 35S::*Citrine* plants in which *Citrine* was expressed from a constitutively active 35S promoter. The 15-day-old plants were cut into two halves. One was used as a control and the other half was used for the gemma cup removal experiments. The cell area of the dorsal epidermal cells at the tip, middle, and base regions for each sample were counted. n = 25 cells of 12 thalli. ns, not significant (p > 0.05), Student's t test.

(M) Two maturation and aging trajectories of the main plant body of *M. polymorpha*. On the top, a schematic of dormant gemmae (the day 0 sample) and thalli spanning various developmental stages (from the D1 to D31 samples). Please note that plant morphology changes over time. On the bottom, a stacking schematic of gemmae and thalli at all developmental stages. Two maturation and aging trajectories of the main plant body of *Marchantia* are inferred. The first trajectory is the gradual maturation of tissues and organs along the tip-to-base axis of the midvein and the second trajectory is the progressive decline of meristem activities in the tip (notch, dashed line) along the chronological axis. The latter aging axis is temporally correlated with the formation of the gemma cups. See also Figure S6.

- Gemma cup removal experiment
- Scanning electron microscope (SEM) and transmission electron microscope (TEM)
- Preparation of protoplasts for scRNA-seq
- scRNA-seq library construction
- Pre-processing of raw scRNA-seq data
- Data integration, clustering, and annotation
- Correlation analysis
- Subclustering
- Gene-ontology enrichment analysis
- Scissor analysis

● QUANTIFICATION AND STATISTICAL ANALYSIS

SUPPLEMENTAL INFORMATION

Supplemental information can be found online at <https://doi.org/10.1016/j.devcel.2023.05.014>.

ACKNOWLEDGMENTS

We thank Dr. Ling Li (Shanghai Jiaotong University, China) for *M. polymorpha* plants; Dr. Wei-Bing Yang and Dr. Dai-Yin Chao (SIPPE, CAS) for discussion; Dr. Tian-Qi Zhang (Nanjing Agricultural University, China) for help in scRNA-seq; and Zhi-Ping Zhang, Xiao-Yan Gao, and Ji-Qin Li (Core Facility of CEMPS, CAS) for technical support in SEM and TEM. This work was supported by grants from the National Natural Science Foundation of China (32388201; 31721001), the Strategic Priority Research Program of the Chinese Academy of Sciences (XDB27030101), and the New Cornerstone Science Foundation through the XPLORER PRIZE.

AUTHOR CONTRIBUTIONS

L.W. and J.-W.W. designed the research. L.W., R.-Y.L., H.-C.X., and Y.-X.M. performed experiments. L.W., M.-C.W., J.X., and Z.-G.X. performed bioinformatic analysis. L.W. and J.-W.W. analyzed the data. J.-W.W. wrote the manuscript.

DECLARATION OF INTERESTS

The authors declare no competing interests.

Received: November 29, 2022

Revised: April 13, 2023

Accepted: May 19, 2023

Published: June 14, 2023

REFERENCES

1. Donoghue, P.C.J., Harrison, C.J., Paps, J., and Schneider, H. (2021). The evolutionary emergence of land plants. *Curr. Biol.* 31, R1281–R1298. <https://doi.org/10.1016/j.cub.2021.07.038>.
2. Bowman, J.L. (2022). The origin of a land flora. *Nat. Plants* 8, 1352–1369. <https://doi.org/10.1038/s41477-022-01283-y>.
3. McDaniel, S.F. (2021). Bryophytes are not early diverging land plants. *New Phytol.* 230, 1300–1304. <https://doi.org/10.1111/nph.17241>.
4. Shimamura, M. (2016). *Marchantia polymorpha*: taxonomy, phylogeny and Morphology of a Model System. *Plant Cell Physiol.* 57, 230–256. <https://doi.org/10.1093/pcp/pcv192>.
5. Chang, C., Bowman, J.L., and Meyerowitz, E.M. (2016). Field guide to plant model systems. *Cell* 167, 325–339. <https://doi.org/10.1016/j.cell.2016.08.031>.
6. Ishizaki, K., Nishihama, R., Yamato, K.T., and Kohchi, T. (2016). Molecular genetic tools and techniques for *Marchantia polymorpha* research. *Plant Cell Physiol.* 57, 262–270. <https://doi.org/10.1093/pcp/pcv097>.
7. Bowman, J.L., Kohchi, T., Yamato, K.T., Jenkins, J., Shu, S., Ishizaki, K., Yamaoka, S., Nishihama, R., Nakamura, Y., Berger, F., et al. (2017). Insights into land plant evolution garnered from the *Marchantia polymorpha* genome. *Cell* 171, 287–304.e15. <https://doi.org/10.1016/j.cell.2017.09.030>.
8. Bowman, J.L., Arteaga-Vazquez, M., Berger, F., Briginshaw, L.N., Carella, P., Aguilar-Cruz, A., Davies, K.M., Dierschke, T., Dolan, L., Dorantes-Acosta, A.E., et al. (2022). The renaissance and enlightenment of *Marchantia* as a model system. *Plant Cell* 34, 3512–3542. <https://doi.org/10.1093/plcell/koac219>.
9. Bowman, J.L. (2022). The liverwort *Marchantia polymorpha*, a model for all ages. *Curr. Top. Dev. Biol.* 147, 1–32. <https://doi.org/10.1016/bs.ctdb.2021.12.009>.
10. Bowman, J.L., Sakakibara, K., Furumizu, C., and Dierschke, T. (2016). Evolution in the cycles of life. *Annu. Rev. Genet.* 50, 133–154. <https://doi.org/10.1146/annurev-genet-120215-035227>.
11. Streubel, S., Deiber, S., Rötzer, J., Mosiolek, M., Jandrasits, K., and Dolan, L. (2023). Meristem dormancy in *Marchantia polymorpha* is regulated by a liverwort-specific miRNA and a clade III SPL gene. *Curr. Biol.* 33, 660–674.e4. <https://doi.org/10.1016/j.cub.2022.12.062>.
12. Kato, H., Yasui, Y., and Ishizaki, K. (2020). Gemma cup and gemma development in *Marchantia polymorpha*. *New Phytol.* 228, 459–465. <https://doi.org/10.1111/nph.16655>.
13. Komatsu, A., Kodama, K., Mizuno, Y., Fujibayashi, M., Naramoto, S., and Kyozuka, J. (2023). Control of vegetative reproduction in *Marchantiapolymerpha* by the KAI2-ligand signaling pathway. *Curr. Biol.* S0960–9822, 00162–00168. <https://doi.org/10.1016/j.cub.2023.02.022>.
14. Honkanen, S., Thamm, A., Arteaga-Vazquez, M.A., and Dolan, L. (2018). Negative regulation of conserved RSL class I bHLH transcription factors evolved independently among land plants. *eLife* 7, e38529. <https://doi.org/10.7554/eLife.38529>.
15. Honkanen, S., Jones, V.A.S., Morieri, G., Champion, C., Hetherington, A.J., Kelly, S., Proust, H., Saint-Marcoux, D., Prescott, H., and Dolan, L. (2016). The mechanism forming the cell surface of tip-growing rooting cells is conserved among land plants. *Curr. Biol.* 26, 3238–3244. <https://doi.org/10.1016/j.cub.2016.09.062>.
16. Jones, V.A., and Dolan, L. (2017). MpWIP regulates air pore complex development in the liverwort *Marchantia polymorpha*. *Development* 144, 1472–1476. <https://doi.org/10.1242/dev.144287>.
17. Proust, H., Honkanen, S., Jones, V.A., Morieri, G., Prescott, H., Kelly, S., Ishizaki, K., Kohchi, T., and Dolan, L. (2016). RSL Class I genes controlled the development of epidermal structures in the common ancestor of land plants. *Curr. Biol.* 26, 93–99. <https://doi.org/10.1016/j.cub.2015.11.042>.
18. Romani, F., Banić, E., Florent, S.N., Kanazawa, T., Goodger, J.Q.D., Mentink, R.A., Dierschke, T., Zachgo, S., Ueda, T., Bowman, J.L., et al. (2020). Oil body formation in *Marchantia polymorpha* is controlled by MpC1HDZ and serves as a defense against arthropod herbivores. *Curr. Biol.* 30, 2815–2828.e8. <https://doi.org/10.1016/j.cub.2020.05.081>.
19. Thamm, A., Saunders, T.E., and Dolan, L. (2020). MpFEW RHIZOIDS1 miRNA-mediated lateral inhibition controls rhizoid cell patterning in *Marchantia polymorpha*. *Curr. Biol.* 30, 1905–1915.e4. <https://doi.org/10.1016/j.cub.2020.03.032>.
20. Kanazawa, T., Morinaka, H., Ebine, K., Shimada, T.L., Ishida, S., Minamino, N., Yamaguchi, K., Shigenobu, S., Kohchi, T., Nakano, A., and Ueda, T. (2020). The liverwort oil body is formed by redirection of the secretory pathway. *Nat. Commun.* 11, 6152. <https://doi.org/10.1038/s41467-020-19978-1>.
21. Yasui, Y., Tsukamoto, S., Sugaya, T., Nishihama, R., Wang, Q., Kato, H., Yamato, K.T., Fukaki, H., Mimura, T., Kubo, H., et al. (2019). GEMMA CUP-ASSOCIATED MYB1, an ortholog of axillary meristem regulators, is essential in vegetative reproduction in *Marchantia polymorpha*. *Curr. Biol.* 29, 3987–3995.e5. <https://doi.org/10.1016/j.cub.2019.10.004>.

22. Rhee, S.Y., Birnbaum, K.D., and Ehrhardt, D.W. (2019). Towards building a plant cell atlas. *Trends Plant Sci.* 24, 303–310. <https://doi.org/10.1016/j.tplants.2019.01.006>.
23. Rich-Griffin, C., Stechemesser, A., Finch, J., Lucas, E., Ott, S., and Schäfer, P. (2020). Single-cell transcriptomics: A high-resolution avenue for plant functional genomics. *Trends Plant Sci.* 25, 186–197. <https://doi.org/10.1016/j.tplants.2019.10.008>.
24. Birnbaum, K.D. (2018). Power in numbers: single-cell RNA-seq strategies to dissect complex tissues. *Annu. Rev. Genet.* 52, 203–221. <https://doi.org/10.1146/annurev-genet-120417-031247>.
25. Rodriguez-Villalon, A., and Brady, S.M. (2019). Single cell RNA sequencing and its promise in reconstructing plant vascular cell lineages. *Curr. Opin. Plant Biol.* 48, 47–56. <https://doi.org/10.1016/j.pbi.2019.04.002>.
26. Liu, Z., Zhou, Y., Guo, J., Li, J., Tian, Z., Zhu, Z., Wang, J., Wu, R., Zhang, B., Hu, Y., et al. (2020). Global dynamic molecular profiling of stomatal lineage cell development by single-cell RNA sequencing. *Mol. Plant* 13, 1178–1193. <https://doi.org/10.1016/j.molp.2020.06.010>.
27. Mironova, V., and Xu, J. (2019). A single-cell view of tissue regeneration in plants. *Curr. Opin. Plant Biol.* 52, 149–154. <https://doi.org/10.1016/j.pbi.2019.09.003>.
28. Eklund, D.M., Kanei, M., Flores-Sandoval, E., Ishizaki, K., Nishihama, R., Kohchi, T., Lagercrantz, U., Bhalerao, R.P., Sakata, Y., and Bowman, J.L. (2018). An evolutionarily conserved abscisic acid signaling pathway regulates dormancy in the liverwort *Marchantia polymorpha*. *Curr. Biol.* 28, 3691–3699.e3. <https://doi.org/10.1016/j.cub.2018.10.018>.
29. Montgomery, S.A., Tanizawa, Y., Galik, B., Wang, N., Ito, T., Mochizuki, T., Akimcheva, S., Bowman, J.L., Cognat, V., Maréchal-Drouard, L., et al. (2020). Chromatin organization in early land plants reveals an ancestral association between H3K27me3, transposons, and constitutive heterochromatin. *Curr. Biol.* 30, 573–588.e7. <https://doi.org/10.1016/j.cub.2019.12.015>.
30. Stuart, T., Butler, A., Hoffman, P., Hafemeister, C., Papalexi, E., Mauck, W.M., 3rd, Hao, Y., Stoeckius, M., Smibert, P., and Satija, R. (2019). Comprehensive integration of single-cell data. *Cell* 177, 1888–1902.e21. <https://doi.org/10.1016/j.cell.2019.05.031>.
31. Satija, R., Farrell, J.A., Gennert, D., Schier, A.F., and Regev, A. (2015). Spatial reconstruction of single-cell gene expression data. *Nat. Biotechnol.* 33, 495–502. <https://doi.org/10.1038/nbt.3192>.
32. Becht, E., McInnes, L., Healy, J., Dutertre, C.A., Kwok, I.W.H., Ng, L.G., Ginhoux, F., and Newell, E.W. (2018). Dimensionality reduction for visualizing single-cell data using tSNE. *Nat. Biotechnol.* 37, 38–44. <https://doi.org/10.1038/nbt.4314>.
33. van der Maaten, L., and Hinton, G. (2008). Visualizing data using t-SNE. *J. Mach. Learn. Res.* 9, 2579–2605.
34. Schönherr, J., and Ziegler, H. (1975). Hydrophobic cuticular ledges prevent water entering the air pores of liverwort thalli. *Planta* 124, 51–60. <https://doi.org/10.1007/BF00390067>.
35. McConaha, M. (1941). Ventral structures effecting capillarity in the Marchantiales. *Am. J. Bot.* 28, 301–306.
36. Westermann, J., Streubel, S., Franck, C.M., Lentz, R., Dolan, L., and Boisson-Dernier, A. (2019). An evolutionarily conserved receptor-like kinases signaling module controls cell wall integrity during tip growth. *Curr. Biol.* 29, 3899–3908.e3. <https://doi.org/10.1016/j.cub.2019.09.069>.
37. Zhang, T.Q., Chen, Y., and Wang, J.W. (2021). A single-cell analysis of the Arabidopsis vegetative shoot apex. *Dev. Cell* 56, 1056–1074.e8. <https://doi.org/10.1016/j.devcel.2021.02.021>.
38. Zhang, T.Q., Chen, Y., Liu, Y., Lin, W.H., and Wang, J.W. (2021). Single-cell transcriptome atlas and chromatin accessibility landscape reveal differentiation trajectories in the rice root. *Nat. Commun.* 12, 2053. <https://doi.org/10.1038/s41467-021-22352-4>.
39. Zong, J., Wang, L., Zhu, L., Bian, L., Zhang, B., Chen, X., Huang, G., Zhang, X., Fan, J., Cao, L., et al. (2022). A rice single cell transcriptomic atlas defines the developmental trajectories of rice floret and inflorescence meristems. *New Phytol.* 234, 494–512. <https://doi.org/10.1111/nph.18008>.
40. Xu, X., Crow, M., Rice, B.R., Li, F., Harris, B., Liu, L., Demesa-Arevalo, E., Lu, Z., Wang, L., Fox, N., et al. (2021). Single-cell RNA sequencing of developing maize ears facilitates functional analysis and trait candidate gene discovery. *Dev. Cell* 56, 557–568.e6. <https://doi.org/10.1016/j.devcel.2020.12.015>.
41. Kubo, H., Nozawa, S., Hiwatashi, T., Kondou, Y., Nakabayashi, R., Mori, T., Saito, K., Takanashi, K., Kohchi, T., and Ishizaki, K. (2018). Biosynthesis of riccionidins and marchantins is regulated by R2R3-MYB transcription factors in *Marchantia polymorpha*. *J. Plant Res.* 131, 849–864. <https://doi.org/10.1007/s10265-018-1044-7>.
42. Jahan, A., Yamazaki, Y., Islam, M., Ghosh, T.K., Yoshimura, N., Kato, H., Ishizaki, K., Shinozawa, A., Sakata, Y., and Takezawa, D. (2022). Differential regulations of abscisic acid-induced desiccation tolerance and vegetative dormancy by group B3 Raf kinases in liverworts. *Front. Plant Sci.* 13, 952820. <https://doi.org/10.3389/fpls.2022.952820>.
43. Sun, D., Guan, X., Moran, A.E., Wu, L.Y., Qian, D.Z., Schedin, P., Dai, M.S., Danilov, A.V., Alumkal, J.J., Adey, A.C., et al. (2022). Identifying phenotype-associated subpopulations by integrating bulk and single-cell sequencing data. *Nat. Biotechnol.* 40, 527–538. <https://doi.org/10.1038/s41587-021-01091-3>.
44. Lockhart, J.A., and Gottschall, V. (1961). Fruit-induced & apical senescence in *Pisum sativum* L. *Plant Physiol.* 36, 389–398. <https://doi.org/10.1104/pp.36.4.389>.
45. Hensel, L.L., Nelson, M.A., Richmond, T.A., and Bleecker, A.B. (1994). The fate of inflorescence meristems is controlled by developing fruits in *Arabidopsis*. *Plant Physiol.* 106, 863–876.
46. Murneek, A.E. (1926). Effects of correlation between vegetative and reproductive functions in the tomato (*Lycopersicon esculentum* Mill.). *Plant Physiol.* 1, 3–56.7. <https://doi.org/10.1104/pp.1.1.3>.
47. Wuest, S.E., Philipp, M.A., Guthörl, D., Schmid, B., and Grossniklaus, U. (2016). Seed production affects maternal growth and senescence in *Arabidopsis*. *Plant Physiol.* 171, 392–404. <https://doi.org/10.1104/pp.15.01995>.
48. Noodén, L.D., and Penney, J.P. (2001). Correlative controls of senescence and plant death in *Arabidopsis thaliana* (Brassicaceae). *J. Exp. Bot.* 52, 2151–2159.
49. Valentine, J.W., Collins, A.G., and Meyer, C.P. (1994). Morphological complexity increase in metazoans. *Paleobiology* 20, 131–142.
50. Deline, B., Greenwood, J.M., Clark, J.W., Puttick, M.N., Peterson, K.J., and Donoghue, P.C.J. (2018). Evolution of metazoan morphological disparity. *Proc. Natl. Acad. Sci. USA* 115, E8909–E8918. <https://doi.org/10.1073/pnas.1810575115>.
51. Denyer, T., Ma, X., Klesen, S., Scacchi, E., Nieselt, K., and Timmermans, M.C.P. (2019). Spatiotemporal developmental trajectories in the *Arabidopsis* Root revealed using high-throughput single-cell RNA sequencing. *Dev. Cell* 48, 840–852.e5. <https://doi.org/10.1016/j.devcel.2019.02.022>.
52. Jean-Baptiste, K., McFaline-Figueredo, J.L., Alexandre, C.M., Dorrrity, M.W., Saunders, L., Bubb, K.L., Trapnell, C., Fields, S., Queitsch, C., and Cuperus, J.T. (2019). Dynamics of gene expression in single root cells of *Arabidopsis thaliana*. *Plant Cell* 31, 993–1011. <https://doi.org/10.1105/tpc.18.00785>.
53. Roszak, P., Heo, J.O., Blob, B., Toyokura, K., Sugiyama, Y., de Luis Balaguer, M.A., Lau, W.W.Y., Hamey, F., Cirrone, J., Madej, E., et al. (2021). Cell-by-cell dissection of phloem development links a maturation gradient to cell specialization. *Science* 374, eaba5531. <https://doi.org/10.1126/science.aba5531>.
54. Shaham, R., Hsu, C.W., Nolan, T.M., Cole, B.J., Taylor, I.W., Greenstreet, L., Zhang, S., Afanassiev, A., Vlot, A.H.C., Schiebinger, G., et al. (2022). A single-cell *Arabidopsis* root atlas reveals developmental trajectories in wild-type and cell identity mutants. *Dev. Cell* 57, 543–560.e9. <https://doi.org/10.1016/j.devcel.2022.01.008>.
55. Zhang, T.Q., Xu, Z.G., Shang, G.D., and Wang, J.W. (2019). A single-cell RNA sequencing profiles the developmental landscape of *Arabidopsis* Root. *Mol. Plant* 12, 648–660. <https://doi.org/10.1016/j.molp.2019.04.004>.

56. Ryu, K.H., Huang, L., Kang, H.M., and Schiefelbein, J. (2019). Single-cell RNA sequencing resolves molecular relationships among individual plant cells. *Plant Physiol.* 179, 1444–1456. <https://doi.org/10.1104/pp.18.01482>.
57. Apelt, F., Mavrothalassiti, E., Gupta, S., Machin, F., Olas, J.J., Annunziata, M.G., Schindelasch, D., and Kragler, F. (2022). Shoot and root single cell sequencing reveals tissue- and daytime-specific transcriptome profiles. *Plant Physiol.* 188, 861–878. <https://doi.org/10.1093/plphys/kiab537>.
58. Zalewski, C.S., Floyd, S.K., Furumizu, C., Sakakibara, K., Stevenson, D.W., and Bowman, J.L. (2013). Evolution of the class IV HD-zip gene family in streptophytes. *Mol. Biol. Evol.* 30, 2347–2365. <https://doi.org/10.1093/molbev/mst132>.
59. Xu, B., Taylor, L., Pucker, B., Feng, T., Glover, B.J., and Brockington, S.F. (2021). The land plant-specific MIXTA-MYB lineage is implicated in the early evolution of the plant cuticle and the colonization of land. *New Phytol.* 229, 2324–2338. <https://doi.org/10.1111/nph.16997>.
60. Hiwatashi, T., Goh, H., Yasui, Y., Koh, L.Q., Takami, H., Kajikawa, M., Kiritu, H., Kanazawa, T., Minamino, N., Togawa, T., et al. (2019). The RopGEF KARAPPO is essential for the initiation of vegetative reproduction in *Marchantia polymorpha*. *Curr. Biol.* 29, 3525–3531.e7. <https://doi.org/10.1016/j.cub.2019.08.071>.
61. Musser, J.M., and Arendt, D. (2017). Loss and gain of cone types in vertebrate ciliary photoreceptor evolution. *Dev. Biol.* 431, 26–35. <https://doi.org/10.1016/j.ydbio.2017.08.038>.
62. Sun, G., Xu, Y., Liu, H., Sun, T., Zhang, J., Hettenhausen, C., Shen, G., Qi, J., Qin, Y., Li, J., et al. (2018). Large-scale gene losses underlie the genome evolution of parasitic plant *Cuscuta australis*. *Nat. Commun.* 9, 2683. <https://doi.org/10.1038/s41467-018-04721-8>.
63. He, X.L., Sun, Y., and Zhu, R.L. (2013). The oil bodies of liverworts: unique and important organelles in land plants. *Crit. Rev. Plant Sci.* 32, 293–302.
64. Balanzà, V., Martínez-Fernández, I., Sato, S., Yanofsky, M.F., Kaufmann, K., Angenent, G.C., Bemer, M., and Ferrández, C. (2018). Genetic control of meristem arrest and life span in *Arabidopsis* by a FRUITFULL-APETALA2 pathway. *Nat. Commun.* 9, 565. <https://doi.org/10.1038/s41467-018-03067-5>.
65. Ware, A., Walker, C.H., Šimura, J., González-Suárez, P., Ljung, K., Bishop, A., Wilson, Z.A., and Bennett, T. (2020). Auxin export from proximal fruits drives arrest in temporally competent inflorescences. *Nat. Plants* 6, 699–707. <https://doi.org/10.1038/s41477-020-0661-z>.
66. Merelo, P., González-Cuadra, I., and Ferrández, C. (2022). A cellular analysis of meristem activity at the end of flowering points to cytokinin as a major regulator of proliferative arrest in *Arabidopsis*. *Curr. Biol.* 32, 749–762.e3. <https://doi.org/10.1016/j.cub.2021.11.069>.
67. Walker, C.H., Ware, A., Šimura, J., Ljung, K., Wilson, Z., and Bennett, T. (2023). Cytokinin signaling regulates two-stage inflorescence arrest in *Arabidopsis*. *Plant Physiol.* 191, 479–495. <https://doi.org/10.1093/plphys/kiac514>.
68. Arendt, D. (2008). The evolution of cell types in animals: emerging principles from molecular studies. *Nat. Rev. Genet.* 9, 868–882. <https://doi.org/10.1038/nrg2416>.
69. Arendt, D., Musser, J.M., Baker, C.V.H., Bergman, A., Cepko, C., Erwin, D.H., Pavlicev, M., Schlosser, G., Widder, S., Laubichler, M.D., and Wagner, G.P. (2016). The origin and evolution of cell types. *Nat. Rev. Genet.* 17, 744–757. <https://doi.org/10.1038/nrg.2016.127>.
70. Tarashansky, A.J., Musser, J.M., Khariton, M., Li, P., Arendt, D., Quake, S.R., and Wang, B. (2021). Mapping single-cell atlases throughout Metazoa unravels cell type evolution. *eLife* 10, e66747. <https://doi.org/10.7554/eLife.66747>.
71. Li, J., Wang, J., Zhang, P., Wang, R., Mei, Y., Sun, Z., Fei, L., Jiang, M., Ma, L., E, W., et al. (2022). Deep learning of cross-species single-cell landscapes identifies conserved regulatory programs underlying cell types. *Nat. Genet.* 54, 1711–1720. <https://doi.org/10.1038/s41588-022-01197-7>.
72. Geirsdottir, L., David, E., Keren-Shaul, H., Weiner, A., Bohlen, S.C., Neuber, J., Balic, A., Giladi, A., Sheban, F., Dutertre, C.A., et al. (2019). Cross-species single-cell analysis reveals divergence of the primate microglia program. *Cell* 179, 1609–1622.e16. <https://doi.org/10.1016/j.cell.2019.11.010>.
73. Wang, J., Sun, H., Jiang, M., Li, J., Zhang, P., Chen, H., Mei, Y., Fei, L., Lai, S., Han, X., et al. (2021). Tracing cell-type evolution by cross-species comparison of cell atlases. *Cell Rep.* 34, 108803. <https://doi.org/10.1016/j.celrep.2021.108803>.
74. Plant Cell Atlas Consortium, Jha, S.G., Borowsky, A.T., Cole, B.J., Fahlgren, N., Farmer, A., Huang, S.C., Karla, P., Libault, M., Provart, N.J., et al. (2021). Vision, challenges and opportunities for a Plant Cell Atlas. *eLife* 10, e66877. <https://doi.org/10.7554/eLife.66877>.
75. Seyfferth, C., Renema, J., Wendrich, J.R., Eekhout, T., Seurinck, R., Vandamme, N., Blob, B., Saeys, Y., Helariutta, Y., Birnbaum, K.D., and De Rybel, B. (2021). Advances and opportunities of single-cell transcriptomics for plant research. *Annu. Rev. Plant Biol.* 72, 847–866. <https://doi.org/10.1146/annurev-aplant-081720-010120>.
76. Chen, S., Zhou, Y., Chen, Y., and Gu, J. (2018). fastp: an ultra-fast all-in-one FASTQ preprocessor. *Bioinformatics* 34, i884–i890. <https://doi.org/10.1093/bioinformatics/bty560>.
77. Kim, D., Paggi, J.M., Park, C., Bennett, C., and Salzberg, S.L. (2019). Graph-based genome alignment and genotyping with HISAT2 and HISAT-genotype. *Nat. Biotechnol.* 37, 907–915. <https://doi.org/10.1038/s41587-019-0201-4>.
78. Leek, J.T., Johnson, W.E., Parker, H.S., Jaffe, A.E., and Storey, J.D. (2012). The sva package for removing batch effects and other unwanted variation in high-throughput experiments. *Bioinformatics* 28, 882–883. <https://doi.org/10.1093/bioinformatics/bts034>.
79. Liao, Y., Smyth, G.K., and Shi, W. (2014). featureCounts: an efficient general purpose program for assigning sequence reads to genomic features. *Bioinformatics* 30, 923–930. <https://doi.org/10.1093/bioinformatics/btt656>.
80. Love, M.I., Huber, W., and Anders, S. (2014). Moderated estimation of fold change and dispersion for RNA-seq data with DESeq2. *Genome Biol.* 15, 550. <https://doi.org/10.1186/s13059-014-0550-8>.
81. Wu, T., Hu, E., Xu, S., Chen, M., Guo, P., Dai, Z., Feng, T., Zhou, L., Tang, W., Zhan, L., et al. (2021). clusterProfiler 4.0: A universal enrichment tool for interpreting omics data. *Innovation (Camb)* 2, 100141. <https://doi.org/10.1016/j.xinn.2021.100141>.
82. Gu, Z., Eils, R., and Schlesner, M. (2016). Complex heatmaps reveal patterns and correlations in multidimensional genomic data. *Bioinformatics* 32, 2847–2849. <https://doi.org/10.1093/bioinformatics/btw313>.
83. Wang, Z.P., Xing, H.L., Dong, L., Zhang, H.Y., Han, C.Y., Wang, X.C., and Chen, Q.J. (2015). Egg cell-specific promoter-controlled CRISPR/Cas9 efficiently generates homozygous mutants for multiple target genes in *Arabidopsis* in a single generation. *Genome Biol.* 16, 144. <https://doi.org/10.1186/s13059-015-0715-0>.
84. Liu, H., Ding, Y., Zhou, Y., Jin, W., Xie, K., and Chen, L.L. (2017). CRISPR-P 2.0: an improved CRISPR-Cas9 tool for genome editing in plants. *Mol. Plant* 10, 530–532. <https://doi.org/10.1016/j.molp.2017.01.003>.
85. Tsuboyama-Tanaka, S., and Kodama, Y. (2015). AgarTrap-mediated genetic transformation using intact gemmae/gemmalings of the liverwort *Marchantia polymorpha* L. *J. Plant Res.* 128, 337–344. <https://doi.org/10.1007/s10265-014-0695-2>.
86. Tanaka, M., Esaki, T., Kenmoku, H., Koeduka, T., Kiyoyama, Y., Masujima, T., Asakawa, Y., and Matsui, K. (2016). Direct evidence of specific localization of sesquiterpenes and marchantin A in oil body cells of *Marchantia polymorpha* L. *Phytochemistry* 130, 77–84. <https://doi.org/10.1016/j.phytochem.2016.06.008>.

STAR★METHODS

KEY RESOURCES TABLE

REAGENT or RESOURCE	SOURCE	IDENTIFIER
Bacterial and virus strains		
<i>Escherichia coli</i> DH5α	N/A	N/A
<i>Agrobacterium tumefaciens</i> GV3101 (pMP90)	N/A	N/A
Chemicals, peptides, and recombinant proteins		
GAMBORG B-5 BASAL MEDIUM	Phyto Technology	Cat#G398
Sucrose	ABCONC	Cat#57501
2-(N-morpholino) ethanesulfonic acid (MES)	BBI Life Sciences	Cat#145224948
Kanamycin sulfate	FCNCS	Cat#M211
Rifampicin solution	FCNCS	Cat#M213
Hygromycin B	YEASEN	Cat#60224ES03
Gentamycin sulfate	FCNCS	Cat#M215
Agar Bacteriological Grade	Shanghai Jiafeng	Cat#H8145
Triton X-100	Sigma-Aldrich	Cat#9002931
Cellulase R10	Yakult Pharmaceutical	Cat#110721-01
Macerozyme R10	Yakult Pharmaceutical	Cat#131126-02
Driselase™ from Basidiomycetes sp. powder	Sigma-Aldrich	Cat#D9515
Snailase	Leagene	Cat#SX7132
EDTA-Na ₂	Sigma-Aldrich	Cat#6381926
Mannitol	Sigma-Aldrich	Cat#M4125
Tris base	Sigma-Aldrich	Cat#77861
Paraplast	Sigma-Aldrich	Cat#P3558
2-mercaptoethanol	Ruibio	Cat#60242
Trypan Blue	Leagene	Cat#CT0030
2 × Phanta® Max Master Mix	Vazyme Biotech	Cat#P515
Phusion High-Fidelity DNA Polymerase	Thermo Fisher Scientific	Cat#022021
Complete Protease Inhibitor Cocktail	Merck	Cat#04693132001
25% glutaraldehyde	Sinopharm Chemical	Cat#01-G0021
Nile red	Yuanye bio	Cat#S19279-100mg
Critical commercial assays		
Chromium Single Cell 3' Gel Bead and Library Kit v3	10 × Genomics	Cat#1000075
CloneExpress II One Step Cloning Kit	Vazyme Biotech	Cat#C11202
NEBNext Ultra II DNA Library Prep Kit for Illumina	New England Biolabs	Cat#E7645S
NEBNext Multiplex Oligos for Illumina	New England Biolabs	Cat#E7335S
Super Plant Genomic DNA kit (polysaccharides & polyphenolics-rich)	TIANGEN	Cat#DP360
RNAprep Pure Plant Plus kit (polysaccharides & polyphenolics-rich)	TIANGEN	Cat#DP441
TruePrep DNA Library Prep Kit v2	Vazyme Biotech	Cat#TD50102
TruePrep Index Kit v2	Vazyme Biotech	Cat#TD202
Deposited data		
scRNA-seq experiment data	This paper	BioProject PRJCA013186, Beijing Institute of Genomics Data Center (http://bigd.big.ac.cn)
RNA-seq experiment data	This paper	BioProject PRJCA013186, Beijing Institute of Genomics Data Center (http://bigd.big.ac.cn)

(Continued on next page)

Continued

REAGENT or RESOURCE	SOURCE	IDENTIFIER
Experimental models: Organisms/strains		
<i>Marchantia polymorpha</i> : Tak-1	N/A	N/A
<i>M. polymorpha</i> : Mp4g12230 knockout mutant	This paper	LW1115
<i>M. polymorpha</i> : Mp3g07510 knockout mutant	This paper	LW1111
<i>M. polymorpha</i> : p35S::Citrine	This paper	LW629
<i>M. polymorpha</i> : pMp5g06510::Citrine	This paper	LW903
<i>M. polymorpha</i> : pMp5g08940::Citrine	This paper	LW940
<i>M. polymorpha</i> : pMp6g16280::Citrine	This paper	LRY247
<i>M. polymorpha</i> : pMp2g13460::Citrine	This paper	LRY011
<i>M. polymorpha</i> : pMp1g28360::Citrine	This paper	LRY05
<i>M. polymorpha</i> : pMp5g09850::Citrine	This paper	LRY328
<i>M. polymorpha</i> : pMp5g09160::Citrine	This paper	LRY327
<i>M. polymorpha</i> : pMp5g04610::Citrine	This paper	LW887
<i>M. polymorpha</i> : pMp7g05980::Citrine	This paper	LRY60
<i>M. polymorpha</i> : pMp4g19900::Citrine	This paper	LW1062
<i>M. polymorpha</i> : pMp3g07510::Citrine	This paper	LW881
<i>M. polymorpha</i> : pMp8g01220::Citrine	This paper	LW894
<i>M. polymorpha</i> : pMp3g15450::Citrine	This paper	LW1054
<i>M. polymorpha</i> : pMp5g10030::Citrine	This paper	LRY067
<i>M. polymorpha</i> : pMp2g25500::Citrine	This paper	LRY065
<i>M. polymorpha</i> : pMp2g14890::MpH2B-Citrine	This paper	LRY417
<i>M. polymorpha</i> : pMp5g19500::Citrine	This paper	LRY280
Oligonucleotides		
See Table S1	N/A	N/A
Software and algorithms		
R v4.2	The R Foundation	RRID: SCR_001905 https://www.r-project.org/
Cell Ranger v3.0.1	10 × Genomics	RRID:SCR_017344 https://support.10xgenomics.com/single-cell-gene-expression/software/pipelines/latest/what-is-cell-ranger
Seurat v3.1.1	Stuart et al. ³⁰	RRID:SCR_016341 https://satijalab.org/seurat/get_started.html
Python v3.7.3	Python Foundation	RRID:SCR_008394 http://www.python.org/
SCISSOR v2.0.0	Sun et al. ⁴³	https://github.com/sunduanchen/Scissor
Plotly v4.9.1	Plotly	RRID:SCR_013991 https://plotly.com/r/
Adobe Photoshop CC 2018	Adobe Acrobat	N/A
Adobe Illustrator CC 2018	Adobe Acrobat	N/A
Fastp v.0.20.0	Chen et al. ⁷⁶	RRID: SCR_016962 https://github.com/OpenGene/fastp
Hisat v2.10.0	Kim et al. ⁷⁷	RRID:SCR_015530 http://ccb.jhu.edu/software/hisat2/index.shtml
sva v3.44.0	Leek et al. ⁷⁸	RRID:SCR_012836 https://git.bioconductor.org/packages/sva
featureCounts v1.6.2	Liao et al. ⁷⁹	RRID: SCR_012919 http://bioinf.wehi.edu.au/featureCounts/
DESeq2 v1.36.0	Love et al. ⁸⁰	RRID: SCR_015687 https://bioconductor.org/packages/release/bioc/html/DESeq2.html
clusterProfiler v4.4.4	Wu et al. ⁸¹	RRID: SCR_016884 https://bioconductor.org/packages/release/bioc/html/clusterProfiler.html

(Continued on next page)

Continued

REAGENT or RESOURCE	SOURCE	IDENTIFIER
complexHeatmap	Gu et al. ⁸²	RRID: SCR_017270 https://jokergoo.github.io/ComplexHeatmap-reference/book/
Other		
Olympus FV3000	Olympus	N/A
Falcon Cell Strainers	Corning	Cat#352340
Chromium Single Cell Instrument	10 × Genomics	N/A
hemocytometer	N/A	N/A
Olympus BX63	Olympus	N/A
TEM	Hitachi	HT7700
SEM	Zeiss	Zeiss Merlin Compact

RESOURCE AVAILABILITY

Lead contact

Further information and requests for resources should be directed to and will be fulfilled by the lead contact, Jia-Wei Wang (jwwang@sippe.ac.cn).

Materials availability

Plasmids and transgenic plant lines generated in this study will be made available on request to the [lead contact](#). This study did not generate new unique reagents.

Data and code availability

- The scRNA-seq and RNA-seq data have been deposited at Beijing Institute of Genomics Data Center (<http://bigd.big.ac.cn>). Accession number is PRJCA013186. Microscopy data reported in this paper will be shared by the [lead contact](#) upon request.
- This paper does not report original code.
- Any additional information required to reanalyze the data reported in this paper is available from the [lead contact](#) upon request.

EXPERIMENTAL MODEL AND SUBJECT DETAILS

The *Marchantia polymorpha* plants (Tak-1) were used for all the experiments. Plants were grown on the half-strength Gamborg B5 solid medium plates supplemented with 1% sucrose at 22°C under continuous light conditions with a light intensity of 80 mmol/m²/s using Philips TLD 36W/865.

METHOD DETAILS

Constructs

To generate promoter Citrine reporters, the upstream regulatory sequences of these genes were PCR-amplified with Phanta High-Fidelity DNA Polymerase (Vazyme, Cat No./ID: P525-02), and cloned into binary construct LW629 in front of the Citrine coding sequence or LW1094 in front of the H2B-Citrine (nuclei-localized Citrine) coding sequence using ClonExpress II One Step Cloning Kit (Vazyme, Cat No./ID: C112-02). For CRISPR/Cas9 constructs, we modified the original PHEE401E construct⁸³: we used *Ubiquitin C* (*Mp3g22950*) promoter to drive the expression of Cas9 and *MpU6* to drive the expression of sgRNAs. The resultant construct was named LW1073. Two sgRNAs for each gene were designed according to a previous study⁸⁴ and cloned into LW1073 ([Figure S3](#)). The primers for cloning were listed in [Table S1](#).

Generation of transgenic plants

The binary constructs were delivered into *Agrobacterium tumefaciens* GV3101 (pMP90) by the freeze-thaw method. Agrobacterium-mediated *M. polymorpha* transformation was performed as previously described with modifications.⁸⁵ Briefly, the gemmae were germinated and grew on the half-strength Gamborg B5 solid medium plates (6 inch) supplemented with 1% sucrose for 6 days, and cultured with Agrobacterium for two days in the dark. The transformants were then selected with 10 mg/mL hygromycin B and 100 mg/mL cefotaxime.

Microscope

The gemmae and thalli were examined under the Olympus FV3000 confocal microscope. The excitation wavelength was 488 nm for Citrine and chlorophyll autofluorescence, and the emission wavelengths were 520 to 550 nm for Citrine or 630 to 730 nm for chlorophyll autofluorescence. Citrine positive cells of the *CYCA1;1::Citrine* reporter near the notch, relative fluorescence intensity, and cell size were measured by ImageJ.

For the measurement of chloroplasts, the tip and base regions of 31-day-old thalli were digested into protoplasts. The oil body cells were stained with Nile Red, which was dissolved in phosphate buffered saline just before use as described.³⁶ The Olympus FV3000 confocal microscope with excitation at 561 nm and emission at 590–650 nm and 670 to 730 nm was used for examining chlorophyll autofluorescence. The chloroplast number and plan area were measured by ImageJ.

Sliced tissues RNA-seq and bulk RNA-seq

For Sliced tissues RNA-seq, the 31-day-old thalli (D31) were sliced into six strips from the tip to base, 1 mm in width (Figure 5C). For bulk RNA-seq, about 100 mg dormant gemmae (D0) or thalli at different developmental stages (D1 to D31) were harvested. Total RNAs were extracted using the RNAPrep Pure Plant Kit (Tiangen, Cat No./ID: DP441). Library construction and deep sequencing were performed using the Illumina NovaSeq Platform according to manufacturer's protocol (Han Yu Biotech, Shanghai, China).

Gemma cup removal experiment

For the experiments described in Figures 7E–7G, we used the #11 blade scalpel to remove all gemma cups on 15-day-old thalli every other day under a stereomicroscope. The thalli of the same size were used as controls. All thalli were photographed after each removal of gemma cups and the blade area were measured with ImageJ. For the experiments described in Figures 7H–7L, the thalli were cut into two halves from the middle. One half was subjected to the gemma cup removal, while the other half was used as a control.

Scanning electron microscope (SEM) and transmission electron microscope (TEM)

For SEM, the thalli samples were frozen in liquid nitrogen and observed under a scanning electron microscope (Zeiss Merlin Compact) using a voltage of 5 kV. For TEM, the samples were fixed in 2.5% (v/v) glutaraldehyde dissolved in phosphate buffered overnight at 4°C. Thin sections were examined under a transmission electron microscope (HT7700, Hitachi) using a voltage of 80 kV.

Preparation of protoplasts for scRNA-seq

The protoplasts were prepared as previously described with modifications.³⁷ Based on the results of our pilot experiments, we found that ~2000 dormant gemmae can yield enough high quality protoplasts for the D0 sample. Briefly, we harvested dormant gemmae and developing thalli at different developmental stages (Figures S1A–S1C). The tissues were separately digested in the RNase-free enzyme solution (3% Cellulase R10, 1% Macerozyme R10, 2% Driselasedriselase, 1% Snailase, 8% mannitol in the half-strength Gamborg B5 liquid media, pH 5.7) for 2 h at room temperature (Figures S1B and S1C). The protoplasts were released by gently shaking, filtered 3–4 times with cell strainers (40 µm in diameter, Falcon, Cat No./ID: 352340), concentrated, and washed 3–4 times with 8% mannitol in the half-strength Gamborg B5 liquid media at room temperature. The protoplast viability was determined by trypan blue staining. The ratio of viable cells to total cells of each sample was higher than 85%. The protoplast suspension was then counted by a hemocytometer. The final concentration of protoplasts was adjusted to 1,500 ~ 2,000 cells/µL.

scRNA-seq library construction

scRNA-seq libraries were prepared as previously described.³⁷ Briefly, the single-cell suspensions were loaded on a Chromium Single Cell Instrument (10x Genomics, Pleasanton, CA) to generate single cell GEMs (Gel Bead in emulsion). scRNA-seq libraries were generated with the Chromium Single Cell 3' Gel Bead and Library Kit v3 (10x Genomics, P/N 1000075, 1000073) according to user guide (10x Genomics, CG000183 Rev A). The DNA libraries were qualified by Agilent 2100 Bioanalyzer and sequenced by Illumina sequencer NovaSeq (Gene Denovo Biotechnology, Guangzhou, China) with read length of 150 bp. The 3' 16 bp 10x Barcode and 10 bp UMI were encoded in Read 1, while Read 2 was used to sequence the complementary DNA fragments. Sample index sequences were incorporated as the i7 index read.

Pre-processing of raw scRNA-seq data

The raw scRNA-seq data were processed as described.³⁷ Briefly, the raw data files were first analyzed by Cell Ranger 3.0.1 (10x Genomics). The genome and GTF annotation files of the *Marchantia* Tak-1 reference genome V5.1 revision 1 were downloaded from marchantia.info (<https://marchantia.info>). The "cellranger mkref" function with "-genome, -fasta and -genes" arguments was used to build reference. The "cellranger count" with "-id, -transcriptome, -fastqs, -sample and -r2-length=98" arguments was performed to generate single-cell gene counts. The ratio of the number of fraction reads in cells to total number of reads for each sample was more than 80%. The Cell Ranger reports were given in Table S1. The gene-cell matrices (named 'filtered_gene_bc_matrices' by 10x Genomics) were used as processed raw data for downstream analyses.

Data integration, clustering, and annotation

We used the Seurat (v.3.1.1) package to perform downstream analyses according to our previous study.³⁷ Briefly, analytic procedures included quality control, data normalization, detection of variable genes, data scaling, PCA analysis, constructing the Shared Nearest Neighbor graph and cell clustering, and data visualization with non-linear dimensional reduction algorithms.

For quality control, low-quality cells and genes were filtered according to following three criteria: (1) the cells in which numbers of expressed genes was less than 500 or higher than 10,000 were filtered; (2) the cells with UMLs above 50,000 and below 500 were filtered; (3) the genes that were expressed in fewer than 3 cells were filtered.

For data normalization, we used the "NormalizeData" function with LogNormalize method and scaling factor of 10,000. We detected variable genes by the "FindVariableFeatures" used selection.method = 'mean.var.plot', mean.cutoff = c(0.0125, 3), dispersion.cutoff = c(1.5, Inf). We then used the "ScaleData" function for data scaling. For the PCA analysis, we used the "RunPCA" function with variable genes and 100 principal components. We further used the "FindNeighbors" and "FindClusters" functions (resolution = 0.5) to construct the SNN graph and clustering cells based on Louvain. Finally, we visualized the data by non-linear dimensional reduction algorithms ("RunUMAP" function, reduction = "pca", dims = 100, n.neighbors = 30L, metric = "correlation", min.dist = 0.3).

To construct a 3D UMAP embedding, three UMAP dimensions were retrieved by "RunUMAP" function with the parameter (n.components = 3). The 3D UMAP scatter graph was then plotted with three UMAP dimensions ('UMAP_1', 'UMAP_2', 'UMAP_3') using the plotly package (v.4.9.1).

The cluster-enriched genes were computed using "FindAllMarkers" function in Seurat with following parameters: a Wilcoxon Rank Sum test; above 1.5-fold difference (logfc.threshold = 0.58) between the two groups of cells; test genes that a minimum fraction was at least 0.25. The well-characterized marker genes among the cluster-enriched genes were then used to annotate cell cluster.

To evaluate the effect of mitochondrial genes on cell clustering, we downloaded the mitochondrion complete genome of *M. polymorpha* subsp. *ruderaleis* strain KBDI00084. The gtf annotation files (<https://www.ncbi.nlm.nih.gov/nuccore/MK202951.1>) were merged with the *Marchantia* Tak-1 reference genome. The dead cells with more than 10% mitochondrial gene sequences were filtered. The downstream analyses were performed as described above. Using a similar approach, we evaluated the effect of protoplasting-induced genes on cell clustering.

Correlation analysis

After using fastp (v.0.20.0) to remove sequencing adapter sequences,⁷⁶ the bulk RNA-seq data were aligned to the reference genome (*M. polymorpha*, Tak-1 V5.1) using Hstat (v2.10.0).⁷⁷ Gene quantification was performed using FeatureCounts (1.6.2),⁷⁹ and the resulting gene expression matrix was imported into R (4.2). The DESeq2 (1.36.0) normalization method was used to normalize the gene expression matrix.⁸⁰ Meanwhile, the single-cell transcriptome data were transformed into pseudo-bulk data and the sva (3.44.0) tool was employed to minimize the batch effects between bulk and pseudo-bulk data.⁷⁸ Finally, Spearman correlation coefficient between the two datasets was calculated by R and visualized with ComplexHeatmap tool.⁸²

Subclustering

The oil body cells (cluster 18) and the meristematic cells near the notch (cluster 11) were extracted. The raw counts were loaded into Seurat to create new Seurat objects. The analyses were performed as described above. The parameters of total number of PCs (npcs), dimensions (dims), the number of neighboring points (n.neighbors), resolution and minimum distance (min.dist) were: npcs = 100, dims = 100, n.neighbors = 30, resolution = 0.5, min.dist = 0.3. After subclustering, the cluster-enriched genes were computed using the "FindAllMarkers" function with following parameters: a Wilcoxon Rank Sum test; above 0.58-fold difference (logfc.threshold = 0.58); 0.25-fold minimum fraction (min.pct = 0.25).

Gene-ontology enrichment analysis

We first identified the orthologous cluster-enriched genes and cluster-highly expressed genes in *A. thaliana* using the Blast algorithm. The resultant genes were subjected to the GO enrichment analysis with clusterProfiler v4.4.4.⁸¹ Fifteen GO terms with $-\log_{10}$ FDR values were given. All the GO terms were listed in Table S1.

Scissor analysis

We used Scissor with default arguments to identify cell subpopulations from single-cell data that are positively or negatively associated with the time series of the liverwort growth stage.⁴³ Briefly, after removing the underlying batch effect by quantifying normalization on the single-cell expression matrix of thalli and aforementioned bulk RNA-seq datasets, a Pearson's correlation matrix of common genes among each pair of cells and bulk RNA-seq samples was calculated. Subsequently, Scissor yielded a regression model on the Pearson matrix with the progressive aging phenotype (i.e., D1, D3, D6, D11, and D31). The cell subpopulations whose transcriptional patterns are significantly positively and negatively associated with the aging phenotype were assigned as the Scissor⁺ and Scissor⁻ cells, respectively (alpha = 0.05, family = "cox", P-value \leq 0.05; The calculation method of statistical significance is provided by Sun et al.⁴³).

QUANTIFICATION AND STATISTICAL ANALYSIS

Two-tailed Student's *t*-test was used to determine the statistical significance between different samples in quantification and phenotypes. For *t*-test, *P*-value < 0.05 is considered as statistical significance, otherwise it will be noted as "ns" for no significant difference. All statistic results and graphs were generated by GraphPad Prism 8 (www.graphpad.com). The numbers of samples and types of statistical analyses are given in figure legends and results sections. No methods were used to determine whether the data met assumptions of the statistical approach.